

DETERMING MOHO DEPTH ACROSS MONTANA USING RECEIVER FUNCTIONS:
IMPLICATIONS FOR THE EXISTENCE OF A HIGH VELOCITY LOWER CRUSTAL
LAYER BENEATH THE STATE OF MONTANA

By

ROBERT THOMAS SIRIANNI

A THESIS PRESENTED TO THE GRADUATE SCHOOL
OF THE UNIVERSITY OF FLORIDA IN PARTIAL FULFILLMENT
OF THE REQUIREMENTS FOR THE DEGREE OF
MASTER OF SCIENCE

UNIVERSITY OF FLORIDA
2010

© 2010 Robert Thomas Sirianni

To my wonderful Mother and Millie

ACKNOWLEDGMENTS

I would like to thank my advisor for his guidance and wisdom throughout my tenure at the University of Florida. I thank my committee members for their advice throughout my research. My mother has been an inspiration to me and has helped me throughout my college career and I thank her for that. My undergraduate advisor must be thanked, even though he brought me into the research world with a terrible dose of MatLab. To my friends here and back home: Elle, Jeremy, Howard, Buddy, TJ, Elliott, Carlos, Ander, and Derrick.

I would also like to thank ExxonMobil for the motivation to finish this project.

TABLE OF CONTENTS

	<u>page</u>
ACKNOWLEDGMENTS.....	4
LIST OF TABLES.....	7
LIST OF FIGURES.....	8
LIST OF ABBREVIATIONS.....	12
ABSTRACT.....	13
CHAPTER	
1 INTRODUCTION.....	15
1.1 Deep Probe-SAREX Projects.....	15
1.2 Geologic Setting.....	18
1.2.1 Precambrian.....	18
1.2.2 Phanerozoic Tectonics.....	19
2 BACKGROUND.....	25
2.1 Development of Receiver Functions.....	25
2.2 How Receiver Functions Work.....	25
2.3 Moho Depth Determination.....	27
3 METHODS.....	32
3.1 Data Collection.....	32
3.2 Filtering.....	32
3.3 Receiver Function and Moho Depth Determination.....	33
4 RESULTS.....	36
4.1 BOZ (Bozeman, Montana).....	36
4.2 DGMT (Dagmar, Montana).....	36
4.3 EGMT (Eagleton, Montana).....	36
4.4 LAO (LASA Array, Montana).....	37
4.5 MSO (Missoula, Montana).....	37
4.6 RLMT (Red Lodge, Montana).....	37
5 DISCUSSION.....	67
5.1 Basin vs. Range.....	67
5.2 EGMT.....	68
5.3 Vp/Vs.....	69

5.4 Previous Publications.....	69
6 CONCLUSIONS.....	74
APPENDIX	
REFERENCE LIST.....	76
BIOGRAPHICAL SKETCH.....	81

LIST OF TABLES

<u>Table</u>	<u>page</u>
3-1 Events listed by date, Julian day (last two digits of the year followed by the day starting from 001 on January first), location, depth and magnitude.....	35
4-1 Location of seismometers, number of events used for each stack and resulting crustal thicknesses and V_p/V_s ratios.....	44

LIST OF FIGURES

<u>Figure</u>	<u>page</u>
1-1 Seismic refraction results (a) and interpretation (b) from Gorman et al. (2002). There is a relatively thick (~25 km), seismically fast (7-8 km/sec) lower crustal layer located between 42-50°N. Latitudes are located at the top of (a) and (b). This layer was interpreted to represent Proterozoic underplating (purple); however, more detail and better resolution is needed for this layer on the US side.....	21
1-2 Map of the study area with the MHB and WC outlined in their general location. The GFTZ is shown in between with a relatively undefined boundary. The triangles are approximate locations for the transportable array seismic stations of the EarthScope project (modified from Foster et al., 2006).....	22
1-3 General location map of the six stations used in this study. RLMT – Red Lodge, Montana; BOZ – Bozeman, Montana; MSO – Missoula, Montana; EGMT – Eagleton, Montana; DGMT – Dagmar, Montana; LAO – LASA Array, Montana. The red line indicates the location of the Deep Probe-SAREX projects. There were only two shots on the U.S. side and thus only a simplified 2-D model could be created, which lacks resolution needed to see the 7x layer. The distribution of the six stations for this proposed project provide a much better idea of the layer's lateral extent.....	23
1-4 Plate convergence vectors during the Sevier (~150-80 Ma) and Laramide orogenies (~80-50 Ma). North America's motion relative to its western subduction margin changed from northwesterly during the Sevier orogeny to west-northwesterly during the Laramide orogeny (modified from Bird, 1998)..	24
2-1 Receiver function example. Resulting seismogram shown at the top with only P-to-S converted waves after the initial P-wave arrival. The bottom diagram represents multiple reflected phases from a single layer model corresponding to the seismogram above (modified from Ammon et al., 1990).....	31
4-1 Six RFs for BOZ. X-axis is time (s), starting at 0 with the initial P-wave arrival, while the Y-axis is ground displacement. Julian Days and BAZ for the events are as follows: 1. 08150, 34.85; 2. 07043, 56.78; 3. 07095, 63.79; 4. 07184, 95.67; 5. 04320, 133.52; 6. 07320, 138.12.....	39
4-2 Six RFs for BOZ. Station X-axis is time (s), starting at 0 with the initial P-wave arrival, while the Y-axis is ground displacement. Julian Days and BAZ for the events are as follows: 7. 07318, 140.81; 8. 07343, 235.33; 9. 07353, 303.07; 10. 08123, 303.16; 11. 07119, 304.09; 12. 0713, 307.86.....	40

4-3	Six RFs for BOZ. X-axis is time (s), starting at 0 with the initial P-wave arrival, while the Y-axis is ground displacement. Julian Days and BAZ for the events are as follows: 13. 05288, 308.58; 14. 07197, 309.62; 15. 07197, 311.31; 16. 08187, 315.73; 17. 06142, 319.32; 18. 08133, 330.26.....	41
4-4	Radial and transverse RF stacks for BOZ. The radial stack includes the previous 18 receiver functions from 4-1 through 4-3.	42
4-5	Stacking results for BOZ using the $s(H,\kappa)$ equation described in 2.3. The star represents the values of crustal thickness and V_p/V_s ratio that maximize the equation. $H = 42.5$ km, $\kappa = 1.95$	43
4-6	Seven RFs for DGMT. X-axis is time (s), starting at 0 with the initial P-wave arrival, while the Y-axis is ground displacement. Julian Days and BAZ for the events are as follows: 1. 08150, 38.09; 2. 07043, 62.15; 3. 07095, 69.45; 4. 07184, 101.66; 5. 04320, 143.75; 6. 05269, 147.29; 7. 07320, 147.45.....	45
4-7	Seven RFs for DGMT. X-axis is time (s), starting at 0 with the initial P-wave arrival, while the Y-axis is ground displacement. Julian Days and BAZ for the events are as follows: 8. 07318, 147.57; 9. 07343, 240.74; 10. 06288, 254.14; 11. 08123, 303.24; 12. 07353, 303.40; 13. 07119, 304.37; 14. 07013, 310.46.	46
4-8	Seven RFs for DGMT. X-axis is time (s), starting at 0 with the initial P-wave arrival, while the Y-axis is ground displacement. Julian Days and BAZ for the events are as follows: 15. 06319, 311.41; 16. 07197, 313.77; 17. 07197, 315.69; 18. 08187, 317.69; 19. 06110, 319.57; 20. 08175, 334.60; 21. 08133, 336.43.....	47
4-9	Radial and transverse RF stacks for DGMT. The radial stack includes the previous 21 receiver functions from 4-6 through 4-8.	48
4-10	Stacking results for DGMT using the $s(H,\kappa)$ equation described in 2.3. The star represents the values of crustal thickness and V_p/V_s ratio that maximize the equation. $H = 40$ km, $\kappa = 1.66$	49
4-11	Four radial RFs for EGMT. X-axis is time (s), starting at 0 with the initial P-wave arrival, while the Y-axis is ground displacement. Julian Days and BAZ for the events are as follows: 1. 08150, 36.50; 2. 07043, 58.59; 3. 07095, 65.92; 4. 08133, 331.89.....	50
4-12	Radial and transverse RF stacks for EGMT. The radial stack includes the previous 4 receiver functions from 4-11.	51
4-13	Five RF functions for EGMT. X-axis is time (s), starting at 0 with the initial P-wave arrival, while the Y-axis is ground displacement. Julian Days and BAZ for the events are as follows: 1. 08123, 301.57; 2. 07013, 307.74; 3. 06319, 308.69; 4. 07197, 312.12; 5. 08187, 315.43.....	52

4-14 Radial and transverse RF stacks for EGMT. The radial stack includes the previous 5 receiver functions from 4-13.	53
4-15 Stacking results for EGMT using the $s(H,\kappa)$ equation described in 2.3. The star represents the values of crustal thickness and V_p/V_s ratio that maximize the equation. This particular model for EGMT used 4 events with BAZ from the NE and NNW. $H = 52$ km, $\kappa = 1.94$	54
4-16 Stacking results for EGMT using the $s(H,\kappa)$ equation described in 2.3. The star represents the values of crustal thickness and V_p/V_s ratio that maximize the equation. This particular model for EGMT used 5 events with BAZ from the WNW. $H = 29.5$ km, $\kappa = 1.59$	55
4-17 Seven RFs for LAO. X-axis is time (s), starting at 0 with the initial P-wave arrival, while the Y-axis is ground displacement. Julian Days and BAZ for the events are as follows: 1. 08150, 36.61; 2. 07043, 60.29; 3. 07095, 67.23; 4. 07184, 99.79; 5. 04320, 140.36; 6. 07320, 144.47; 7. 05269, 144.50.....	56
4-18 Seven RFs for LAO. X-axis is time (s), starting at 0 with the initial P-wave arrival, while the Y-axis is ground displacement. Julian Days and BAZ for the events are as follows: 8. 07318, 145.56; 9. 06288, 253.79; 10. 08123, 303.98; 11. 07119, 305.01; 12. 07013, 310.09; 13. 05288, 310.79; 14. 06319, 311.01.	57
4-19 Seven RFs for LAO. Station X-axis is time (s), starting at 0 with the initial P-wave arrival, while the Y-axis is ground displacement. Julian Days and BAZ for the events are as follows: 15. 07197, 312.76; 16. 07197, 314.58; 17. 08187, 317.51; 18. 06119, 319.32; 19. 06110, 319.99; 20. 06142, 320.14; 21. 08133, 334.67.....	58
4-20 Radial and transverse RF stacks for LAO. The radial stack includes the previous 21 receiver functions from 4-17 through 4-19.	59
4-21 Stacking results for LAO using the $s(H,\kappa)$ equation described in 2.3. The star represents the values of crustal thickness and V_p/V_s ratio that maximize the equation. $H = 38$ km, $\kappa = 1.62$	60
4-22 Nine RFs for MSO. Station X-axis is time (s), starting at 0 with the initial P-wave arrival, while the Y-axis is ground displacement. Julian Days and BAZ for the events are as follows: 1. 07043, 55.70; 2. 07095, 62.93; 3. 07184, 94.12; 4. 07119, 302.31; 5. 05288, 306.94; 6. 08187, 314.27; 7. 06119, 317.26; 8. 06110, 317.97; 9. 06142, 318.05.....	61
4-23 Radial and transverse RF stacks for MSO. The radial stack includes the previous 9 receiver functions from 4-22.	62
4-24 Stacking results for MSO using the $s(H,\kappa)$ equation described in 2.3. The star represents the values of crustal thickness and V_p/V_s ratio that maximize the equation. $H = 45.5$ km, $\kappa = 1.97$	63

4-25	Eight radial RFs for RLMT. X-axis is time (s), starting at 0 with the initial P-wave arrival, while the Y-axis is ground displacement.....	64
4-26	Eight radial RFs for RLMT. X-axis is time (s), starting at 0 with the initial P-wave arrival, while the Y-axis is ground displacement.....	65
4-27	Radial and transverse RFs stacks for RLMT. The radial stack is comprised of the previous 16 RFs in Figure 4-25 and 4-26. The amplitude is diminished due to the lack of coherence in the individual RFs. The large negative amplitude in the transverse RF is indicative of a complex structure, likely a dipping layer or non horizontal Moho.	66
5-1	Location of EGMT along the Deep Probe-SAREX interpretation. A number of prominent features to the north, including massive folds, are likely the reason for the discrepancy in H values (modified from Gorman et al., 2002).....	73

LIST OF ABBREVIATIONS

BAZ	Back Azimuth – Azimuthal direction from the station to the event
BOZ	Broadband Seismic Station located in Bozeman, Montana
DGMT	Broadband Seismic Station located in Dagmar, Montana
EARS	Earthscope Automated Receiver Survey
EGMT	Broadband Seismic Station located in Eagleton, Montana
GFTZ	Great Falls Tectonic Zone
<i>H</i>	Crustal Thickness
IRIS DMC	Incorporated Research Institutions for Seismology Data Management Center, www.iris.edu
<i>K</i>	V_p/V_s ratio
LAO	Broadband Seismic Station located in the LASA Array, Montana
LCL	Lower Crustal Layer
MHB	Medicine Hat Block
Moho	Mohorovičić discontinuity, seismic velocity/density contrast between the crust and mantle
MSO	Broadband Seismic Station located in Missoula, Montana
RF(s)	Receiver Function(s)
RLMT	Broadband Seismic Station located in Red Lodge, Montana
SAC	Seismic Analysis Code
USNSN	United States National Seismograph Network
WC	Wyoming Craton

Abstract of Thesis Presented to the Graduate School
of the University of Florida in Partial Fulfillment of the
Requirements for the Degree of Master of Science

DETERMINING MOHO DEPTH ACROSS MONTANA USING RECEIVER FUNCTIONS:
IMPLICATIONS FOR THE EXISTENCE OF A HIGH VELOCITY LOWER CRUSTAL
LAYER BENEATH THE STATE OF MONTANA

By

Robert Thomas Sirianni

May 2010

Chair: Raymond M. Russo
Major: Geology

The active source Deep Probe-SAREX projects (Henstock et al., 1998; Clowes et al., 2002; Gorman et al., 2002) imaged a high velocity lower crustal layer (LCL), ~20-35 km thick, within the Wyoming Craton (WC) and Medicine Hat Block (MHB), positioned beneath the states of Wyoming and Montana, and north into Canada, during the Deep Probe-SAREX seismic refraction projects. The layer is relatively thick (~25 km) and propagates *P* waves at velocities between 7-8 km/sec, giving the so-called 7x layer its name. The LCL is not well defined on the north-south Deep Probe-SAREX line in the USA due to poor resolution (shot spacing ~700 km), and the linearity of the seismic sampling does not define the layer's extent to the east or west. We used receiver functions (RFs) at 6 permanent ANSS stations derived from 35 events to determine Moho depth beneath each station. Moho depth determination will help aid in determining whether or not the 7x layer is present at each location. If the crust is thicker than average crustal values or previously reported thicknesses for these stations, it is possible that the layer does exist, on a per station basis. The seismic stations are located across Montana and are the reference points for this study. The RFs resolve

any extant sharp velocity contrast boundaries, such as horizontal and dipping beds and juxtaposed tectonic units. Scattering of P-to-S conversions off these sharp velocity interfaces helped identify the lateral extent of the high velocity lower crustal layer (LCL). Using an algorithm developed by Zhu and Kanamori (2000) it is possible to use the P_s , P_pP_s , and $P_pS_s+P_sP_s$ phases to predict crustal thicknesses and V_p/V_s ratios for these stations.

The results indicate that BOZ and MSO, located in the Northern Rocky Mountains, have, in general, thicker crust and higher V_p/V_s ratios. High V_p/V_s ratios are diagnostic of propagation through mafic crustal rocks and are consistent with the presence of the LCL beneath these two stations. Continental crust at stations DGMT and LAO is thinner and V_p/V_s ratios are lower than at BOZ and MSO. These two stations are situated in the Williston Basin, and sedimentary basins generally are characterized by higher V_p/V_s ratios, but the RF signals at these stations are dominated by the predominately silica-rich basement beneath the Williston Basin strata. The high V_p/V_s ratios of the stations in the Rocky Mountains provide some supporting evidence for a hypothesized mafic underplating event, occurring after the amalgamation of Laurentia was complete.

The crustal thickness results of this study compare well with previous studies throughout the Northern Rocky Mountains. Values, in general, are within a few kilometers of observed receiver function depths. The largest discrepancies arise when structural complexity becomes too significant to ignore in radial receiver function analysis.

CHAPTER 1 INTRODUCTION

1.1 Deep Probe-SAREX Projects

The active source Deep Probe-SAREX projects (Henstock et al., 1998; Clowes et al., 2002; Gorman et al., 2002) identified a fast (> 7 km/sec) lower crustal layer (LCL) beneath the states of Montana and Wyoming, extending into Canada (Figure 1-1). This layer, at depths of 20 to 35 km, is called the 7x layer due to its high P wave velocity, typical of mafic crustal rocks, whereas typical values for lower continental crust range from ~ 6 -7 km/sec (Holbrook et al., 1992). More recently, Rumpfhuber et al. (2009) reanalyzed data from the combined passive and active source CD-ROM (Continental Dynamics of the Rocky Mountain) project (Keller et al., 1999), using receiver functions to delineate crustal structure in some detail from the southern end of the Deep Probe line from central Wyoming to northern New Mexico. They found that the thick, seismically fast LCL extends south of the Deep Probe line to around 42° N latitude along the CD-ROM line, thinning and apparently pinching out southwards beneath the Cheyenne Belt. The LCL is thus clearly not limited latitudinally to one craton, but appears to extend beneath the Wyoming craton (WC), Medicine Hat block (MHB), and the intervening Great Falls tectonic zone (GFTZ; Figure 1-2).

Resolution of the seismic imaging in these studies is highly variable, and resolved structure north of the U.S. border is visibly much more complex (Figure 1-1) where active source shot spacing was closer. Interpretation of the refraction profile on the U.S. side is more problematic, given the much greater distance between refraction shot spacing of the Deep Probe experiment on the U.S. side of the border. The Rumpfhuber et al. (2009) study is similarly low resolution, as its structures derive from RFs at

stations spaced around 20 km apart. The low resolution leaves open the possibility of unresolved tectonic structure within or along the apparently smooth boundaries of the LCL beneath Montana and Wyoming, which could be consistent with a wide range of genetic scenarios.

Gorman et al. (2002) interpreted the LCL to be a result of Proterozoic mafic magmatic underplating of the MHB and WC, based on the ages of two xenoliths from the Sweet Grass Hills complex in northern Montana, dated at 1745 Ma and 1814 Ma. Ross (2002) suggested that these xenoliths originated at depths of 47 and 39 km, the first from the LCL in the MHB, and the second from the Archean portion of the MHB. The separate dates and depths were interpreted by Ross (2002) to indicate a single magmatic underplating event occurred during the Proterozoic. However, Carlson et al. (2004) dated the Williams and Homestead kimberlite xenoliths, in the WC, to be Archean in age. This suggests that the LCL was not emplaced in the area where these kimberlites originated, or it may not exist at all.

The interpretations of Chamberlain et al. (2003) involve two distinct emplacement events for the LCL within the WC – during the Archean at ~2.7 Ga, and the Mesoproterozoic at ~1.5 Ga – and emplacement of yet a third type of LCL within the MHB at ~1.8 Ga. The oldest potential age for the LCL here derives from the 2.7 Ga Stillwater mafic dikes that outcrop throughout the WC (Beartooth, Bighorn, and Owl Creek Mountains). The 2.7 Ga emplacement ages predate the GFTZ suturing and MHB LCL emplacement (~1.8 Ga), implying that the LCLs within the MHB and WC resulted from two separate emplacement events (Snyder et al., 1989; Kirkwood, 2000; Mueller et al., 2002; Chamberlain et al., 2003).

Chamberlain et al. (2003) postulate that the 1.8 Ga xenoliths from the Sweet Grass Hills complex resulted from the Proterozoic suturing of an amalgamated MHB and WC to the Hearne craton, rather than from an underplating event. Chamberlain et al. (2003) further posit that the mafic LCL within the MHB is a structurally complex oceanic crust, subducted and amalgamated to the base of pre-existing MHB crust or lithosphere.

The results of the Deep Probe-SAREX-CD-ROM studies allow all these interpretations because the seismic structure beneath the MHB is complex, with higher velocities and velocity gradients, while the WC LCL seems to be flatter with less deformation between the crust-mantle contact (Figure 1-2). Note that these differences are likely due to resolution differences along the Deep Probe-SAREX line, as mentioned above, given variable shot spacing above each craton. Regardless of the age(s) of the WC and MHB lower crustal layer(s) – 2.7 Ga, 1.8 Ga, or 1.5 Ga – the best seismic data in hand (Gorman et al., 2002; Rumpfhuber et al., 2009) clearly indicate that the layer is anomalously seismically fast and thick, and underlies the MHB, GFTZ, and WC at least from the U.S.-Canada border to south-central Wyoming. High seismic velocities, > 7 km/s, in the lower crust are clearly indicative of the presence of mafic material, and such materials are typically characterized by high (1.7-1.9) V_p/V_s ratios.

In the remainder of this thesis, I present results intended to improve our understanding of the extent of the LCL to the west and east of the Deep Probe-SAREX line in Montana. I determined crustal thickness at six permanent seismic stations (Figure 1-3) using an iterative deconvolution method on earthquake P waves to produce RFs (Ligorría and Ammon, 1999), and an algorithm for simultaneously determining

crustal thickness and Vp/Vs ratio (Zhu & Kanamori, 2000). The algorithm predicts timing of crust-mantle boundary seismic wave conversions and reflections and matches the predicted arrival times to observed converted and reverberating S waves in the receiver functions. The stations used in this study were not chosen by us, but rather provided high-quality freely-available data at the time of this study. Although not ideal, they are widely distributed with respect to the Deep Probe-SAREX-CD-ROM line in the area. Results can be coupled to those of the EarthScope Transportable Array to define boundaries of the LCL.

1.2 Geologic Setting

The tectonic history of the study area is important because the crustal structures and fabrics that may have developed as a result of plate collisions and suturing, extensional tectonics, and magmatism will strongly affect the seismic response at the study stations. Radial RFs are used to image horizontal layers and are modified in systematic ways by departures of the actual structures from horizontal layering (as described in **2.2**). The likely effects of tectonic events that may have altered crustal structures and fabrics must therefore be taken into account when interpreting the results of the RF analyses.

1.2.1 Precambrian

A map of the cratonic assemblage is shown in Figure 1-2. The stations we used are located on the Medicine Hat Block, the Wyoming Craton, and the boundary between them, the Great Falls Tectonic Zone, and on the Trans-Hudson and Selway terranes. Sedimentary cover of the Williston Basin exists just to the east of the Rocky Mountains and deepens on the Trans-Hudson terrane (increasing eastward to ~3500 m; Baird et

al., 1995). The GFTZ is an enigmatic structure: O'Neill and Lopez (1985) and O'Neill (1998) posited that the GFTZ formed when the MHB, already sutured to the Hearne craton, collided with the WC. Alternatively, the WC and MHB had already collided, creating the GFTZ, and this composite then amalgamated to the Hearne craton as a single structure (Boerner et al., 1998). Whether this interaction was strictly collisional or involved significant shear parallel to the GFTZ is unclear. Mueller et al. (2002) used zircon ages with whole-rock Sm-Nd data to hypothesize that the GFTZ is a suture marking the closure of a subducted ocean basin between the MHB and WC at ~1.8 Ga. This suturing would be expected to complicate crustal structure by formation of thrust faults and folds taking up shortening strain between the colliding terranes, and any suture parallel shear would also be expected to modify crustal structures, all of which could have produced structures departing from the simple layering assumed *a priori* in the RF analysis.

1.2.2 Phanerozoic Tectonics

Deformation events in the study region since the Precambrian are dominated – in terms of extant geologic structures today – by the development of subduction beneath western North America (Figure 1-4) and attendant crustal shortening which formed the Cordillera (e.g., Bird 1998; Foster et al., 2006). The Phanerozoic deformation in the Northern Rocky mountains is largely constrained to the Paleoproterozoic and younger terranes surrounding the Archean cratons, although Laramide-age reverse faults are found throughout the WC. These terranes include the GFTZ, Selway, and Farmington zone (Figure 1-2). The Cordilleran fold-thrust belt and Laramide basement uplifts have

involved the most deformation, largely shortening, to the west of the MHB and in the northwestern portion of the WC.

Similarly, the majority of Eocene extension and volcanism has primarily affected Proterozoic and younger structures. The Bitterroot and Anaconda detachments, and the Priest River and Clearwater complexes account for a majority of Eocene extension within the study area. The Lewis and Clark fault zone acted as a connection between these regions of large displacement. The amount of extension ranges from ~65-85 km individually, but as a whole up to ~100 km of extension can be accounted for to the north and south of the Lewis and Clark fault zone (Foster et al., 2007). These structures also produced widespread magmatism as a result of a subducting slab window. This shallowly subducting slab caused asthenospheric upwelling and subsequent partial melting of the lithosphere creating igneous intrusions throughout the aforementioned structures (Foster et al., 2006; Foster et al., 2007).

Archean cratons were likely formed and stabilized by different processes than Proterozoic provinces; however, the exact nature of these processes is debated (O'Neill and Lopez, 1985; O'Neill, 1998; Mueller et al., 2002; Humphreys et al., 2003; Foster et al., 2006; Foster et al., 2007). Differences in the degree and style of deformations and magmatism that affected Proterozoic and Archean lithospheres in the study area may complicate receiver functions, and, consequently, differences in the compositional makeup of each terrane will likely yield various V_p/V_s ratios.

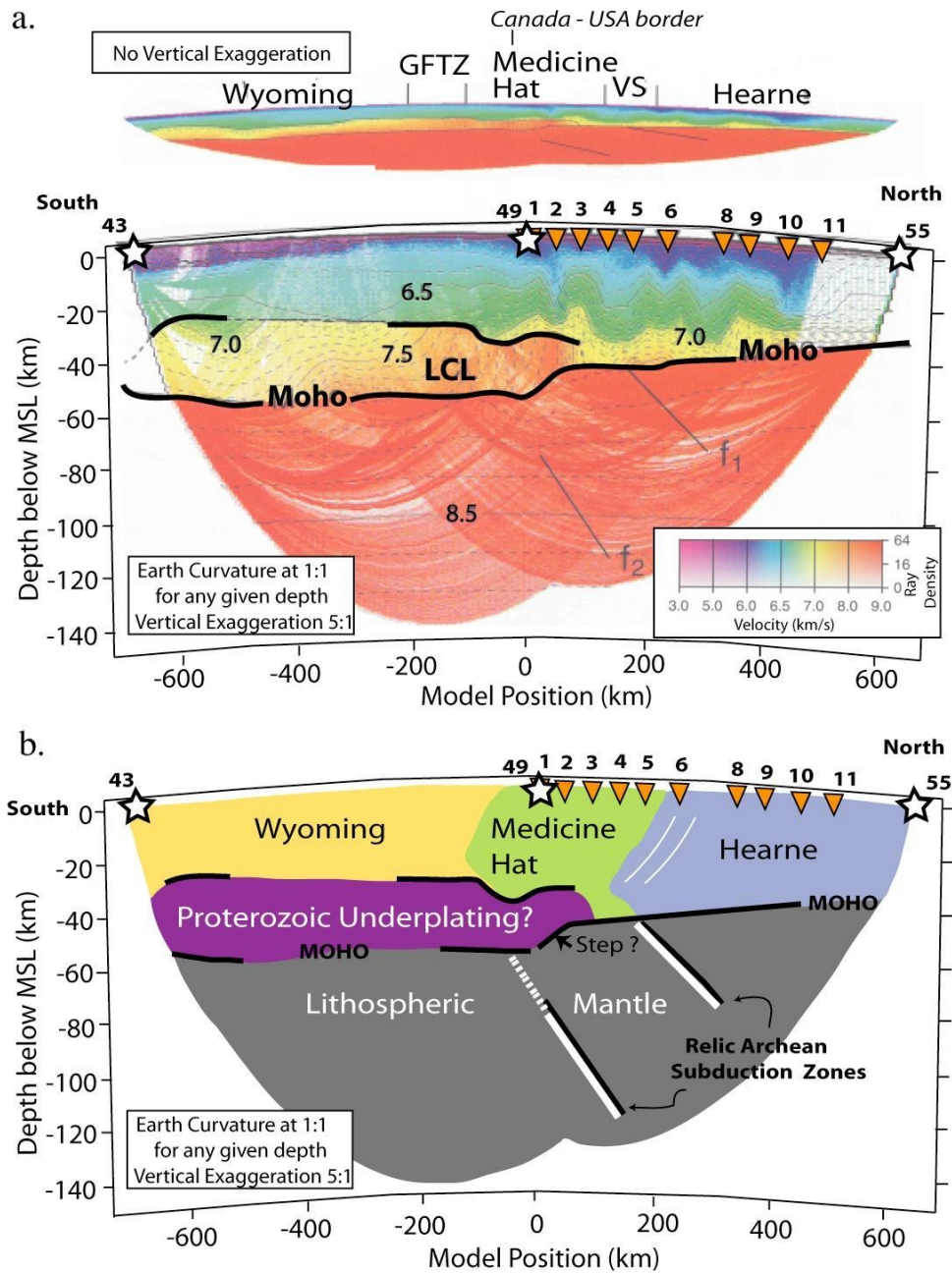


Figure 1-1. Seismic refraction results (a) and interpretation (b) from Gorman et al. (2002). There is a relatively thick (~25 km), seismically fast (7-8 km/sec) lower crustal layer located between 42-50°N. Latitudes are located at the top of (a) and (b). This layer was interpreted to represent Proterozoic underplating (purple); however, more detail and better resolution is needed for this layer on the US side.

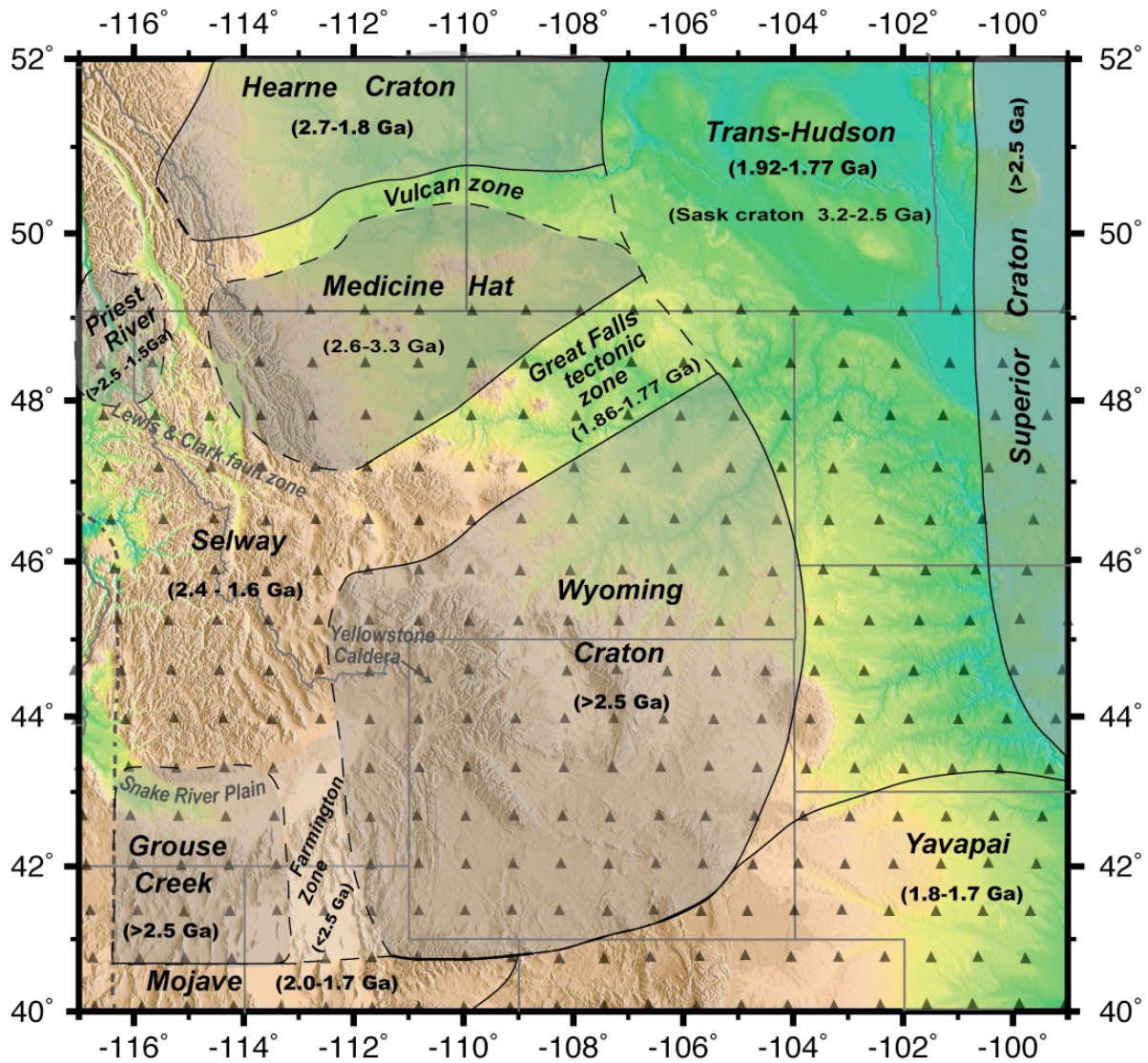


Figure 1-2. Map of the study area with the MHB and WC outlined in their general location. The GFTZ is shown in between with a relatively undefined boundary. The triangles are approximate locations for the transportable array seismic stations of the EarthScope project (modified from Foster et al., 2006).

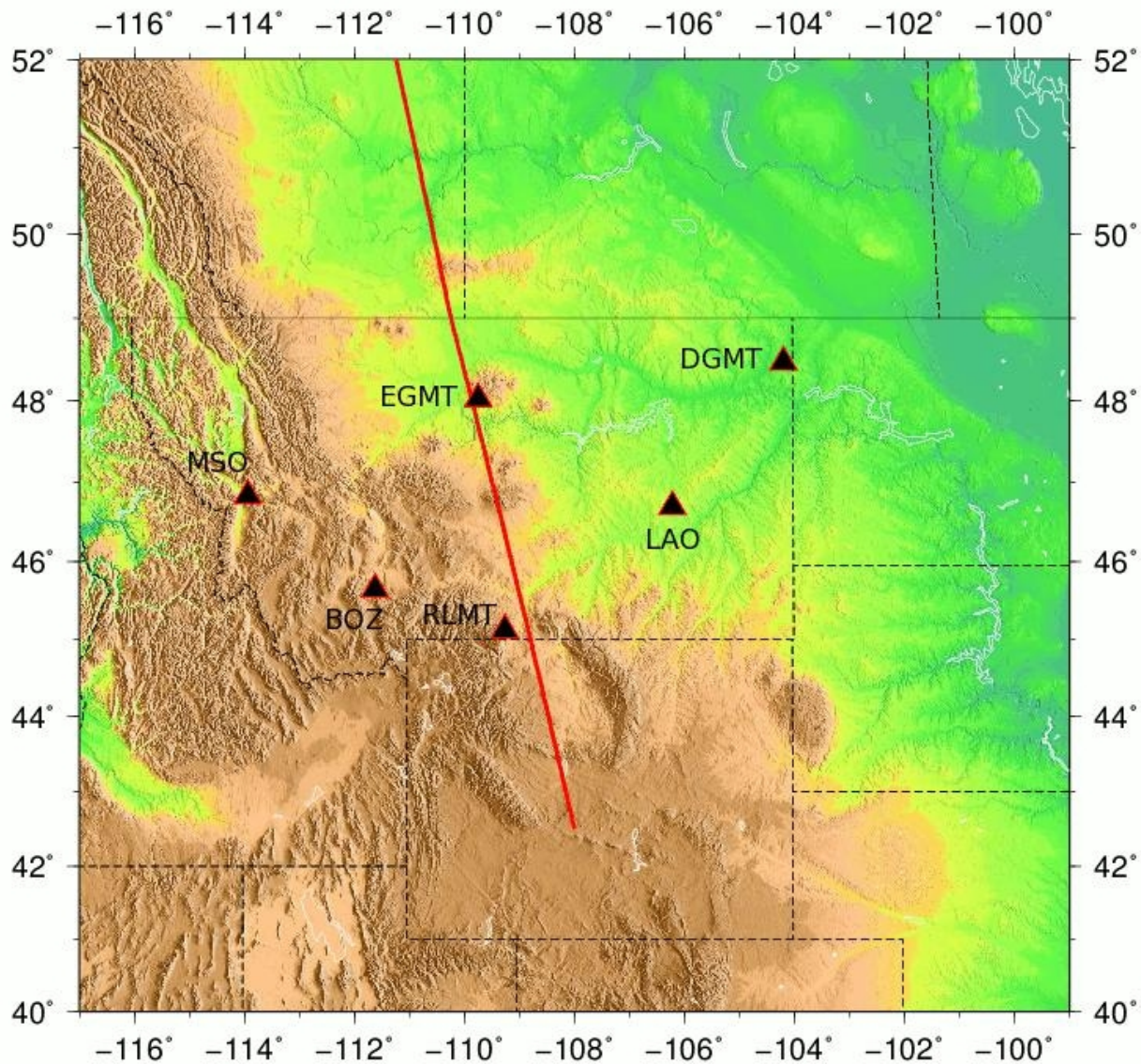


Figure 1-3. General location map of the six stations used in this study. RLMT – Red Lodge, Montana; BOZ – Bozeman, Montana; MSO – Missoula, Montana; EGMT – Eagleton, Montana; DGMT – Dagmar, Montana; LAO – LASA Array, Montana. The red line indicates the location of the Deep Probe-SAREX projects. There were only two shots on the U.S. side and thus only a simplified 2-D model could be created, which lacks resolution needed to see the 7x layer. The distribution of the six stations for this proposed project provide a much better idea of the layer's lateral extent.

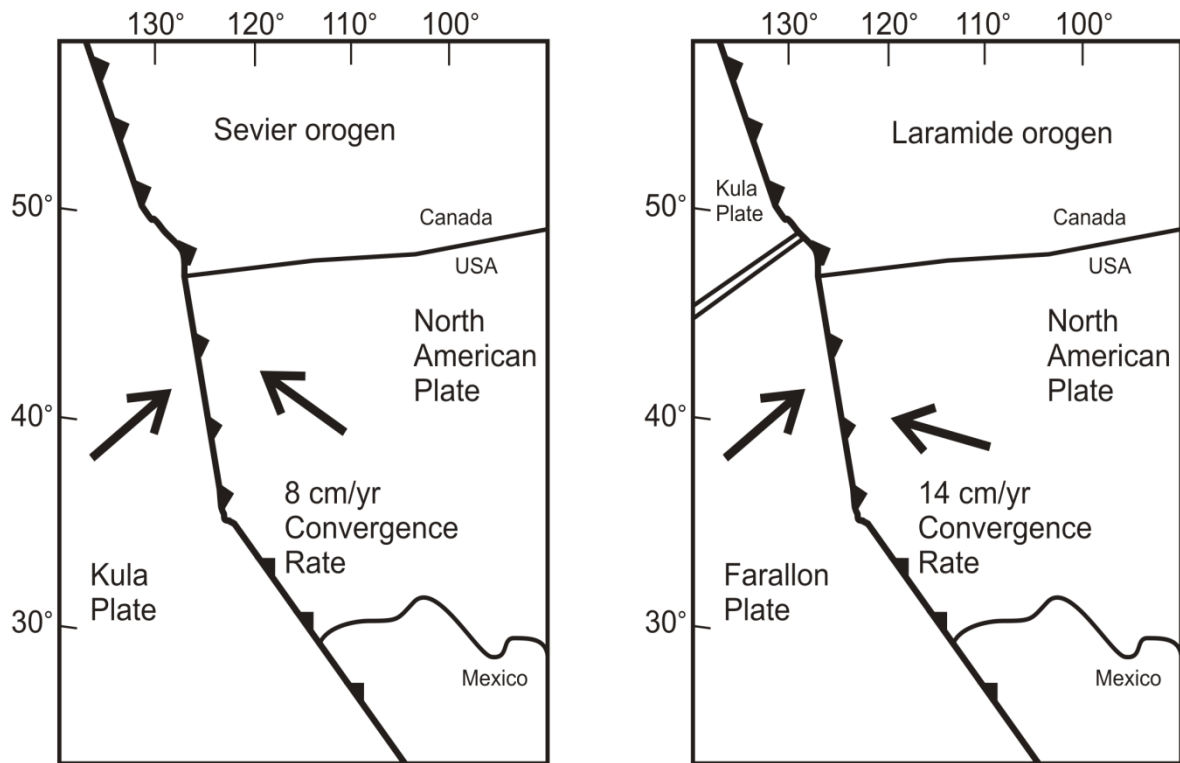


Figure 1-4. Plate convergence vectors during the Sevier (~150-80 Ma) and Laramide orogenies (~80-50 Ma). North America's motion relative to its western subduction margin changed from northwesterly during the Sevier orogeny to west-northwesterly during the Laramide orogeny (modified from Bird, 1998).

CHAPTER 2 BACKGROUND

2.1 Development of Receiver Functions

In 1977 Langston introduced RF analysis as a means to describe crustal and upper mantle structure. His first test of this new technique was to study the structure under Corvallis, Oregon. The results of this work conformed nicely with previous seismic refraction studies (Berg et al., 1966; Johnson and Couch, 1970) and performed better than older spectral interpretations. One of the main advantages to using RFs is the ability to map and detect dipping layers. Langston expanded his work by doing RF studies on crustal structure under Mount Rainier, Washington in 1979, and later seismologists, such as, Ammon (1990, 1991), Cassidy (1992, 1995), and Levin and Park (1997) also expanded and refined Langston's RF method. This method is now accepted and used worldwide.

2.2 How Receiver Functions Work

The approach for a RF is fairly basic. Seismograms are split into two components. The vertical seismogram includes P waves and is interpreted as the direct arrival of these waves. The horizontal component is constructed from two signals recording horizontal ground motion, typically one in the N-S direction and the other oriented E-W. A rotation of these seismograms from these orientations yields the necessary radial and transverse component seismograms, depending on the source-receiver geometry. The radial component seismogram often includes many of the reflected or converted waves, and for the case of RFs we are interested in P -to- S wave conversions and their reverberations in a layered medium such as the crust. These conversions can define boundary layers close to the surface in great detail. P -to- S

wave conversions are generated when an incoming P wave encounters a sharp, high impedance contrast and moves the boundary both in the vertical (propagating the P wave) and horizontal direction, creating an S wave conversion (Stein and Wysession, 2002).

I used an iterative deconvolution method (Ligorria and Ammon, 1999) to model these conversions. The vertical component is cross-correlated with the radial to estimate the lag of the first converted S arrival (typically from the Moho i.e., Mohorovičić discontinuity) for the RF. This step produces the first peak for the RF. The convolution of this RF with the vertical component produces a seismogram that is subtracted from the radial component (i.e., deconvolution). The deconvolution equations are as follows:

$$E_R(\omega) = \frac{(D_R(\omega)D_{Vi}(\omega))}{(\Phi_{SS}(\omega))} * G(\omega) \quad (1)$$

$$\text{where } \Phi_{SS}(\omega) = \max[D_V(\omega)D_{Vi}(\omega), c\max[D_V(\omega)D_{Vi}(\omega)]] \quad (2)$$

$$\text{and } G(\omega) = e^{(-\omega^2/4a^2)} \quad (3)$$

The deconvolved radial earth response is represented by $E_R(\omega)$. The complex conjugate of $D_V(\omega)$ is given by $D_{Vi}(\omega)$ with (ω) denoting the frequency domain. Φ_{SS} is the autocorrelation of $D_V(\omega)$. The parameter c sets the level that fills spectral troughs that may occur. $G(\omega)$ is a Gaussian filter that is controlled by a , the width of the filter. The Gaussian filter has a smooth shape, similar to that of a seismic pulse in the time domain and limits spurious high-frequency signal in the output $E_R(\omega)$ (Langston, 1979).

Simply put, deconvolution is done in the frequency domain because it is easier. In the frequency domain deconvolution is a simple division of the radial by the vertical

component, whereby the P-wave reverberations of the vertical component are “subtracted” out. The following equation demonstrates this division.

$$H(\omega) = \frac{(R(\omega))}{(Z(\omega))} \quad (4)$$

$H(\omega)$ is the receiver function in the frequency domain (Ammon, 1991). Once deconvolved, an inverse Fourier transform is performed to convert back to the time domain (Langston, 1979).

This procedure is repeated to produce spikes appropriately lagged and of proper amplitudes to match all observed arrivals on the radial RF. Eventually, the iterative deconvolution of the vertical component and RF seismogram look similar to the radial component. The process will continue until a user-defined minimum error is reached and the misfit between the convolution produced seismogram and the radial component is insignificant (Ligorria and Ammon, 1999). The resulting RFs are also considered radial and transverse seismograms, with the radial primarily imaging conversions from horizontal layers and the transverse most sensitive to conversions from dipping layers, if present in the subsurface. The radial RF images horizontal layers because of the way the SV wave propagates, and the same is true for the transverse RF and SH waves. The structure being investigated can be mapped by using P and S wave travel times and the output of the RFs, or the P-to-S wave conversions that define the boundaries (Stein and Wysession, 2002; Figure 2-1).

2.3 Moho Depth Determination

A RF provides an estimation of Moho depth by providing an estimate of the delay time between the P and Ps phases with lateral variation minimized due to the steep

incidence angle of the teleseismic wave (Zhu and Kanamori, 2000). However, as shown in this equation,

$$H = \frac{tp_s}{\left(\sqrt{\left(\frac{1}{V_s^2}\right)-p^2}\right) - \sqrt{\left(\frac{1}{V_p^2}\right)-p^2}} \quad (1)$$

the crustal thickness (H) is highly dependent on the S wave velocity (V_s) through the crust. t is the time delay between the P and P_s phases, V_p is the P wave velocity and p is the ray parameter for the incident wave (Zhu and Kanamori, 2000). One way to reduce the ambiguity of the wave velocities is to introduce later P -to- S reverberations and converted phases, including the $PpPs$ and $PpSs+PsPs$ phases. The first P is the incoming wave before it interacts with the crust. The next lower case letter is the transmitted phase at the boundary. For $PpPs$, the incoming P wave shakes the boundary dominantly in the vertical direction producing a transmitted P wave with a strong signal, but if it arrives at an angle other than 90° , a radial component will also be introduced in the form of an S wave. The third letter is the first reflection of the surface and the last letter is the incoming wave to the station as a reflection off of the Moho (Figure 2-1). The sign of the amplitude (positive vs. negative) is determined by reflection polarity changes. When a P -wave reflects off a boundary, the amplitude of the resultant wave has an opposite polarity. An S wave does not undergo this change, thus the P_s and $PpPs$ phases are positive while the $PpSs+PsPs$ phase is negative.

$$H = \frac{(tp_{pPs})}{\left(\sqrt{\left(\frac{1}{V_s^2}\right)-p^2}\right) + \sqrt{\left(\frac{1}{V_p^2}\right)-p^2}} \quad (2)$$

and

$$H = \frac{(t(p_p s_s + p_s p_s))}{(2\sqrt{(\frac{1}{V_s^2} - p^2)})} \quad (3)$$

These two equations introduce more constraints on V_p and V_s so that the V_p/V_s ratio and the crustal thickness can be determined (Zhu, 1993; Zandt et al., 1995; Zandt and Ammon, 1995). In these equations the layer thickness is calculated based on the predicted timing of 2 different phases ($PpPs$ and $PpSs+PsPs$). These times are divided by the the up going ray velocities before interaction with receiver while the ray parameters are subtracted out. The denominators end up as $1/s*v^{-1}$, while the numerators are in s. This gives the predicted thickness for these phases from the Moho to the station.

Stacking of RFs increases signal-to-noise ratio, while reducing lateral variation in the Moho around the station as long as a large azimuthal distribution of events are obtained. Using a single event can produce an anomaly based on the incoming angle. An undulation or fault within the crust may cause mis-timing in peaks and troughs in the seismogram. Using multiple events with different BAZ will suppress these discrepancies, and the stacking of these events will better represent the average structure beneath the station.

Zhu and Kanamori (2000) developed an algorithm that uses stacked receiver functions and outputs crustal thicknesses and V_p/V_s ratios using the following equation:

$$s(H, \kappa) = \omega_1 r(t_1) + \omega_2 r(t_2) - \omega_3 r(t_3) \quad (4)$$

κ represents V_p/V_s , $r(t)$ are the receiver functions where t_1 , t_2 , and t_3 represent the predicted arrival times for Ps , $PpPs$, and $PpSs+PsPs$, and ω_i are weighting factors with

$\sum \omega_i = 1$. Weights of $w_1 = 0.7$, $w_2 = 0.2$, and $w_3 = 0.1$ were used in the stacking to balance the effects from each phase with $w_1 > w_2 + w_3$. The Ps phase is weighted most because it has the highest signal-to-noise ratio and is, therefore, more reliable than the last two phases. The V_p/V_s ratio is a ratio of *P*-wave velocity divided by the *S*-wave velocity through a given medium. V_p/V_s ratios higher than 1.8 are expected for mafic rocks and Williston Basin strata, ratios lower than 1.8 are indicative of felsic-rich rocks (Holbrook et al., 1992; Brauer et al., 2007). Multiple predicted times are used for t_1 , t_2 , and t_3 until a maximum is reached for $s(H, \kappa)$. These predicted times correspond to the 3 phases mentioned above and represent the largest amplitudes on the seismogram for those times. That maximum value of s represents H and κ for that station. Advantages of this method include the ability to process large amounts of data relatively quickly, and arrival times are estimated, eliminating the need to pick phases for each individual seismogram.

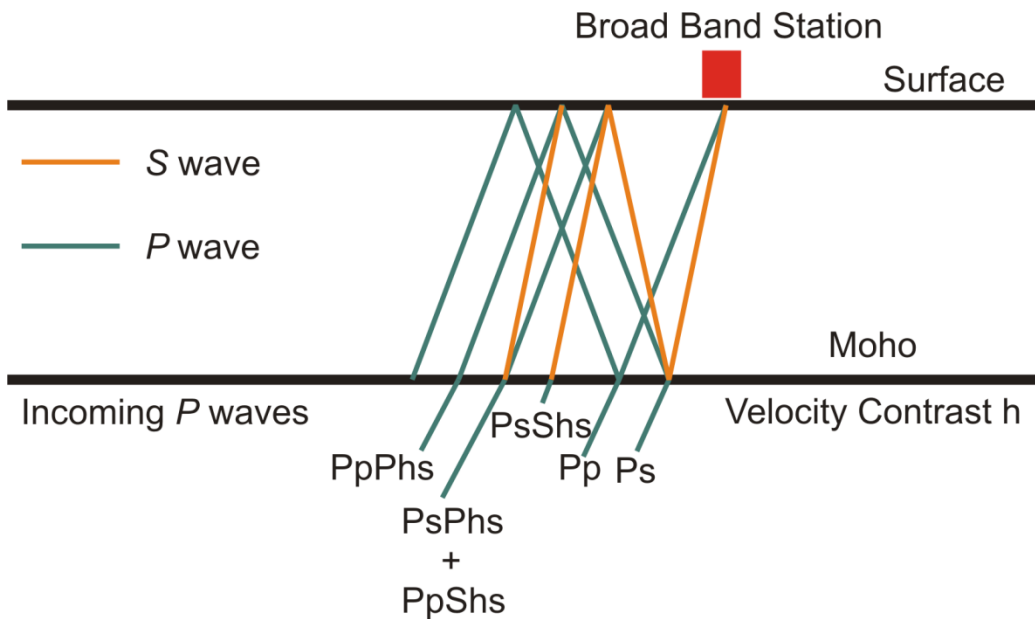
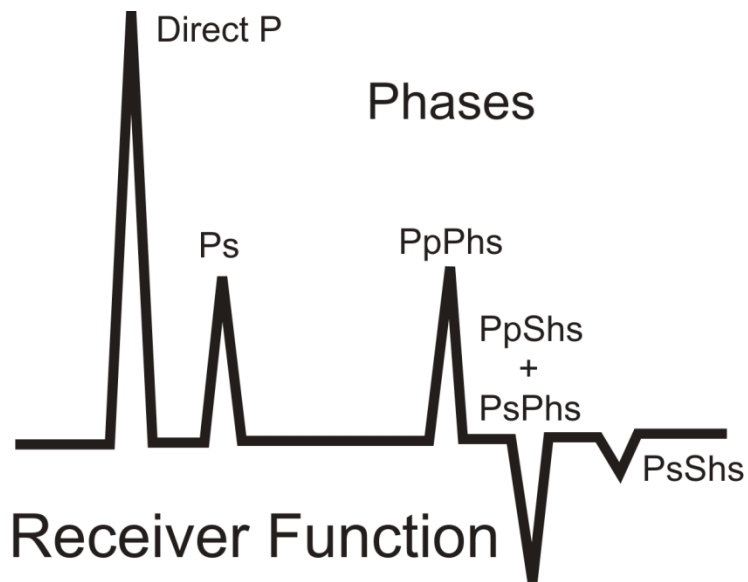


Figure 2-1. Receiver function example. Resulting seismogram shown at the top with only *P*-to-*S* converted waves after the initial *P*-wave arrival. The bottom diagram represents multiple reflected phases from a single layer model corresponding to the seismogram above (modified from Ammon et al., 1990).

CHAPTER 3 METHODS

3.1 Data Collection

The United States National Seismograph Network (USNSN) currently has six permanent broadband stations in Montana. During the time of this study, the EarthScope transportable array was setup in this region; however, the information was not available when data processing began, limiting the project to the six aforementioned stations. Approximately thirty-five seismic events were chosen based on limiting characteristics. RF computation requires that the event has a magnitude of 6.0 or higher to ensure a high signal-to-noise ratio (Table 3-1). To sample the mantle without sampling too deep (i.e., the core) or too shallow, events must have an angular distance of 35-90° from each station. Event numbers were limited based on the date in which each station became active (1999-2006) and matching with the aforementioned criteria. Data collection took place between June and July 2008 from Incorporated Research Institutions for Seismology Data Management Center (www.iris.edu), free-of-charge.

3.2 Filtering

Each event was analyzed using the seismic analysis code (SAC). The analysis includes removing the mean and trend from the seismograms to eliminate any extraneous effects (high frequency noise, earth tides, and/or diurnal temperature fluctuations). I tapered the individual seismograms using a cosine function, which sets the first and last points to zero using a monotonically varying function between zero and one, and I bandpass filtered, which enhances signal-to-noise ratio by eliminating frequencies outside of the pertinent 0.01-0.1 Hz range. Teleseismic signals generally have a frequency inside this range while noise outside this range is eliminated. I cut the

resulting seismograms to 5 seconds before the initial P wave arrival and 55 seconds after, ensuring that conversions from crustal and upper mantle structure were retained in the seismograms for all reasonable seismic velocities. I rotated the east and north components to the radial and transverse, BAZ (Back Azimuth), with the radial component parallel to the BAZ and the transverse perpendicular to this direction.

3.3 Receiver Function and Moho Depth Determination

Ray parameters were calculated for each event/station based on the following equations.

$$p = \frac{1}{c_x} \quad (1)$$

$$\text{where } c_x = \frac{V}{(\sin i)} \quad (2)$$

$$\text{and } V = V_0 + kz \quad (3)$$

p is the ray parameter and c_x is the apparent horizontal velocity. V is the seismic velocity for the ray and i is the incidence angle. V_0 , k and z are the seismic velocity at the surface, a constant and the source depth respectively (Stein and Wysession, 2002).

I then applied the iterative deconvolution method, as described in 2.2. Using the radial RFs it is almost always possible to determine the depth of the Moho at each station, since the P -to- S conversion at the Moho is typically very strong. The conversion is strong due to the impedance contrast between the two media, with the impedance being defined by the velocity and density changes between the media. The larger the changes in these two properties, the larger the impedance contrast (Stein and

Wysession, 2002). By using multiple P-to-S converted phases and stacking the RFs (described in **2.3**), ambiguity in the V_p/V_s ratio is greatly reduced.

Multiple BAZ for various events at a single station will diminish lateral variability in the crust beneath each station, providing a more accurate depth. Clusters for the 35 events were grouped in the Aleutian Islands, Japan, Northern Chile, the Caribbean, and a few along the Mid-Atlantic Ridge (Table 3-1). Event BAZ for each station can be found on the receiver function figures corresponding to that station. Applying the algorithm developed by Zhu and Kanamori (2000) gives a best estimation for H and κ .

Table 3-1. Events listed by date, Julian day (last two digits of the year followed by the day starting from 001 on January first), location, depth and magnitude.

Date	Julian Day	Latitude	Longitude	Depth (km)	Mw
11/15/2004	04320	-5.4300	-77.5100	15.00	7.1
09/26/2005	05269	-5.6800	-76.4000	115.00	7.5
10/15/2005	05288	46.8200	154.1100	42.80	6.1
04/20/2006	06110	60.9500	167.0900	22.00	7.6
04/29/2006	06119	60.4900	167.5200	11.00	6.6
05/22/2006	06142	60.7700	165.7400	16.50	6.6
10/15/2006	06288	19.8800	-155.9400	38.90	6.7
11/15/2006	06319	46.5900	153.2700	10.00	8.3
01/13/2007	07013	46.2400	154.5200	10.00	7.9
02/04/2007	07035	19.3700	-78.5200	10.00	6.2
02/12/2007	07043	35.8000	-10.3300	10.00	5.9
02/14/2007	07045	-29.5900	-112.0500	10.00	5.9
04/05/2007	07095	37.3100	-24.6200	14.00	6.2
04/29/2007	07119	52.0100	-179.9700	117.00	6.2
07/03/2007	07184	0.7200	-30.2700	10.00	6.1
07/16/2007	07197	37.5400	138.4500	12.00	6.5
07/16/2007	07197	36.8100	134.8500	350.40	6.8
07/21/2007	07202	-22.1500	-65.7800	289.50	6.3
11/14/2007	07318	-22.2500	-69.8900	40.00	7.7
11/16/2007	07320	-2.3100	-77.8400	122.90	6.7
12/09/2007	07343	-26.0000	-177.5100	152.50	7.7
12/16/2007	07350	-22.9500	-70.1800	45.00	6.7
12/19/2007	07353	51.3600	-179.5200	29.40	7.0
02/08/2008	08039	10.6700	-41.9000	9.00	6.9
03/24/2008	08084	-20.0400	-68.9600	120.00	6.2
04/15/2008	08106	51.8500	-179.3600	10.00	6.4
04/16/2008	08107	51.8800	-179.1700	13.00	6.6
05/02/2008	08123	51.8600	-177.5300	14.00	6.6
05/09/2008	08130	12.5200	143.1800	76.00	6.7
05/12/2008	08133	31.0000	103.3200	19.00	7.9
05/20/2008	08141	51.1600	178.7600	27.00	6.3
05/23/2008	08144	7.2600	-34.8800	10.00	6.4
05/29/2008	08150	64.0000	-21.0100	10.00	6.2
06/22/2008	08174	67.6700	141.4100	12.60	5.9
07/05/2008	08187	53.8900	153.0300	605.40	7.5

CHAPTER 4 RESULTS

4.1 BOZ (Bozeman, Montana)

BOZ is located on the northwest corner of the WC, just south of the GFTZ (Figure 1-3). The station is situated in the basin and range extensional region of the Northern Rocky Mountain Belt and has been active in the USNSN since 1999. Of the ~35 events that met the criteria mentioned in 3.1, 18 were deemed suitable (handpicked with strong signal-to-noise ratios) for RF processing. The resulting RFs are shown in Figures 4-1 through 4-3 with the stacked RF in Figure 4-4. Maximum values for equation 2.3.4 give a crustal thickness of 42.5 km and a V_p/V_s ratio of 1.95. Figure 4-5 shows the stacking results with warmer colors (yellow to orange) representing maximum values for $s(H,\kappa)$. Table 4-1 has station locations (latitude and longitude), number of events, crustal thicknesses, and V_p/V_s ratios for this station and the following.

4.2 DGMT (Dagmar, Montana)

DGMT is located just northeast of the WC in the Williston Phanerozoic sediments of the Trans-Hudson orogen (Figure 1-3). The station has been active since 2004 and is situated on the Williston Basin. 21 events, from a wide azimuthal distribution, were used to create the RF stack. The resulting RFs and RF stack are shown in Figures 4-6 through 4-9. Crustal thickness for this station is estimated to be 40 km while the V_p/V_s ratio is 1.66.

4.3 EGMT (Eagleton, Montana)

The station is located at the transition between the Northern Rocky Mountains and the Williston Basin and has been active since 2005. This transtional zone, along with tectonic history, has resulted in multiple outputs for H and κ . I looked at two different

azimuthal distributions of events based on similarity of RF outputs. Four RFs were used with BAZ of NNW and NE (Figures 4-11 and 4-12) as well as five RFs with BAZ to the WNW (Figures 4-13 and 4-14). The first set has outputs of $H = 52$ and $\kappa = 1.94$, while the second has $H = 29.5$ and $\kappa = 1.59$ (Figures 4-15 and 4-16).

4.4 LAO (LASA Array, Montana)

The LASA Array station is located on the western edge of the Williston basin, above the WC (Figure 1-3). The station has been active since 2004 in the USNSN and 21 usable RFs were computed (Figures 4-17 through 4-20). The RF stack for this station is shown in Figure 4-20. Calculations for crustal thickness and V_p/V_s ratios give 38 km and 1.62, respectively (Figure 4-21).

4.5 MSO (Missoula, Montana)

MSO is located within the Selway basement, to the west of the GFTZ (Figure 1-3). Similar to BOZ, the Missoula station is situated in the center of the Northern Rocky Mountain Belt. It has been active in the USNSN since 2002. 9 events met the criteria from 3.1 and had strong signal-to-noise ratios. The resulting RFs are shown in Figures 4-22 and the RF stack is shown in Figure 4-23. Maximum values for $s(H,\kappa)$ give a crustal thickness of 45.5 km and a V_p/V_s ratio of 1.97 (Figure 4-24).

4.6 RLMT (Red Lodge, Montana)

RLMT produced low amplitude radial RFs with high amplitude transverse RFs, indicative of complicated structure (i.e., dipping layers of varying orientation) beneath the station (Figures 4-25 through 4-27). RLMT is located in an intermountain basin, NE of the Yellowstone Hotspot (Figure 1-3). Moho depths would be difficult to investigate at

this location due to low amplitudes of the radial RFs and therefore we will not investigate this station further.

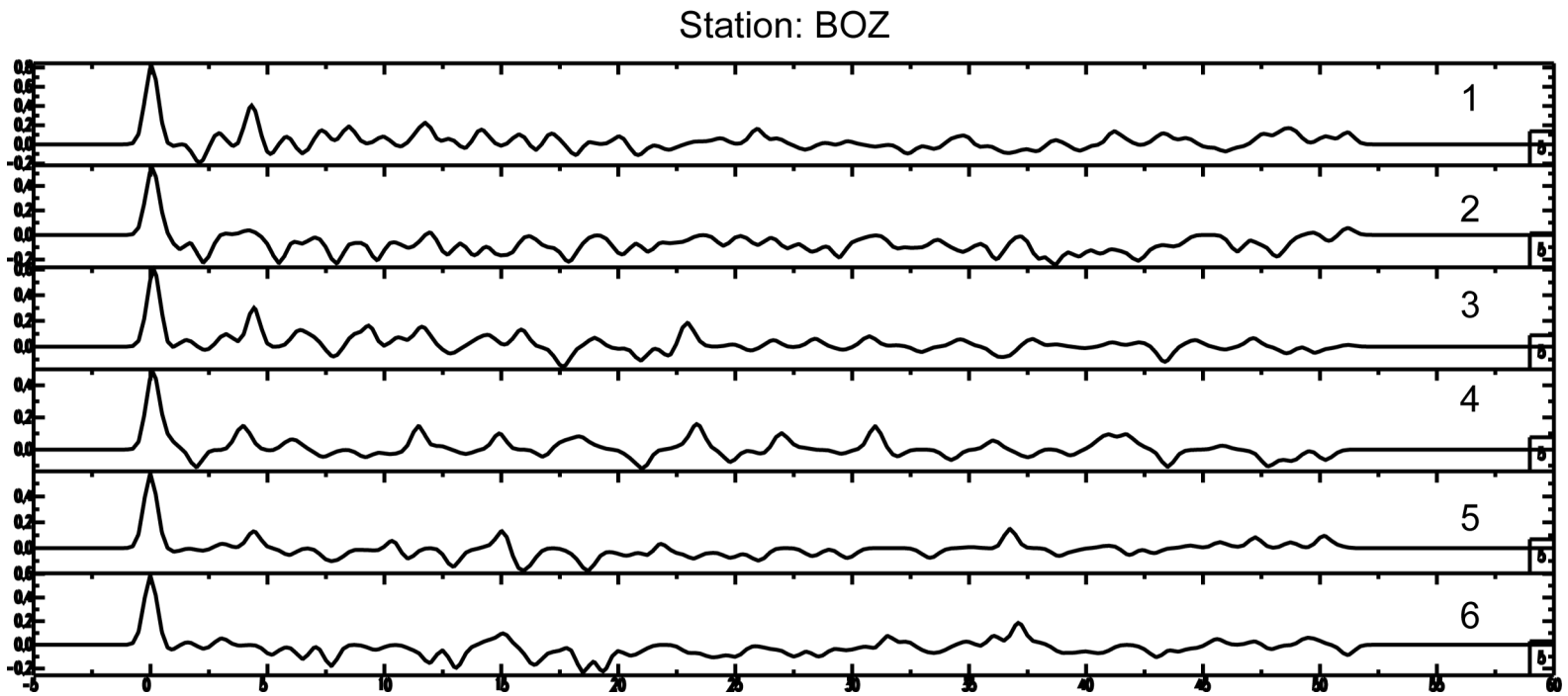


Figure 4-1. Six RFs for BOZ. X-axis is time (s), starting at 0 with the initial *P*-wave arrival, while the Y-axis is ground displacement. Julian Days and BAZ for the events are as follows: 1. 08150, 34.85; 2. 07043, 56.78; 3. 07095, 63.79; 4. 07184, 95.67; 5. 04320, 133.52; 6. 07320, 138.12.

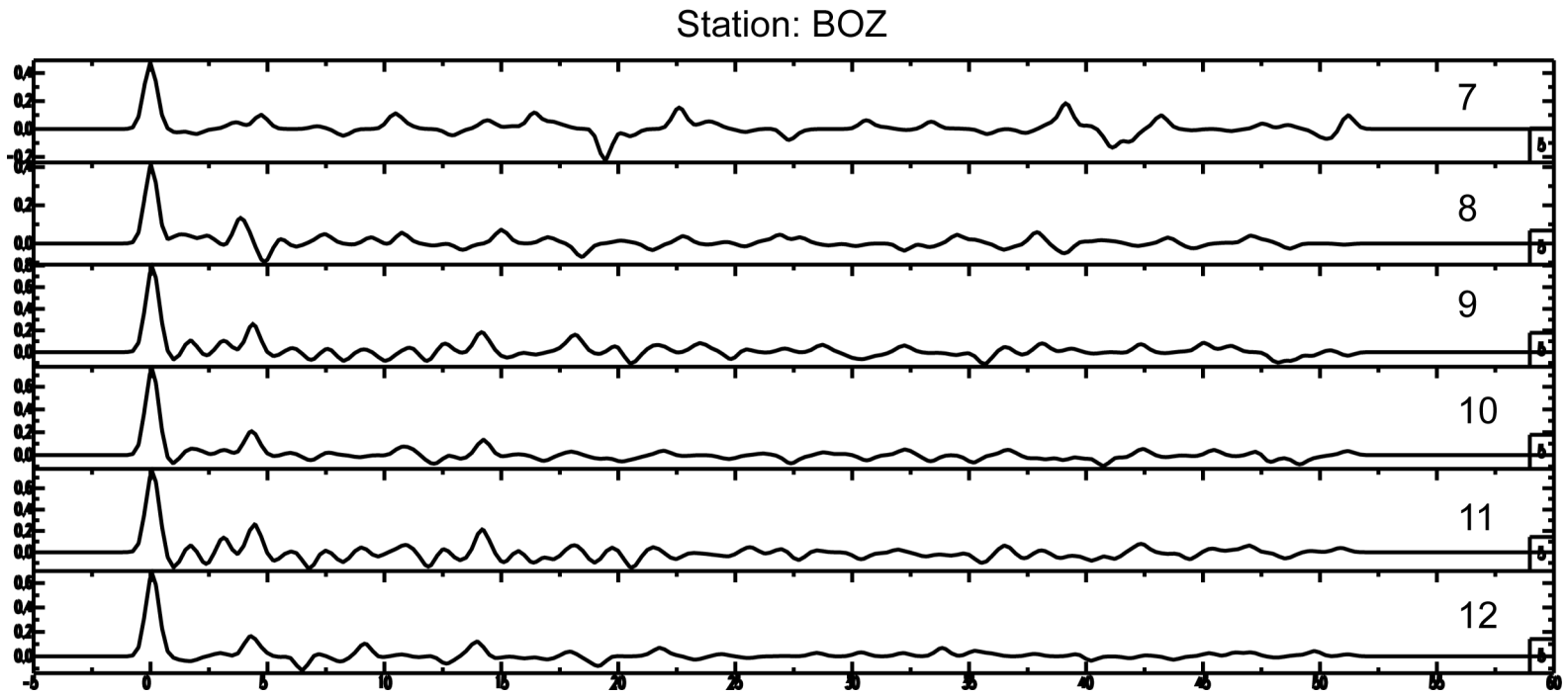


Figure 4-2. Six RFs for BOZ. Station X-axis is time (s), starting at 0 with the initial *P*-wave arrival, while the Y-axis is ground displacement. Julian Days and BAZ for the events are as follows: 7. 07318, 140.81; 8. 07343, 235.33; 9. 07353, 303.07; 10. 08123, 303.16; 11. 07119, 304.09; 12. 0713, 307.86.

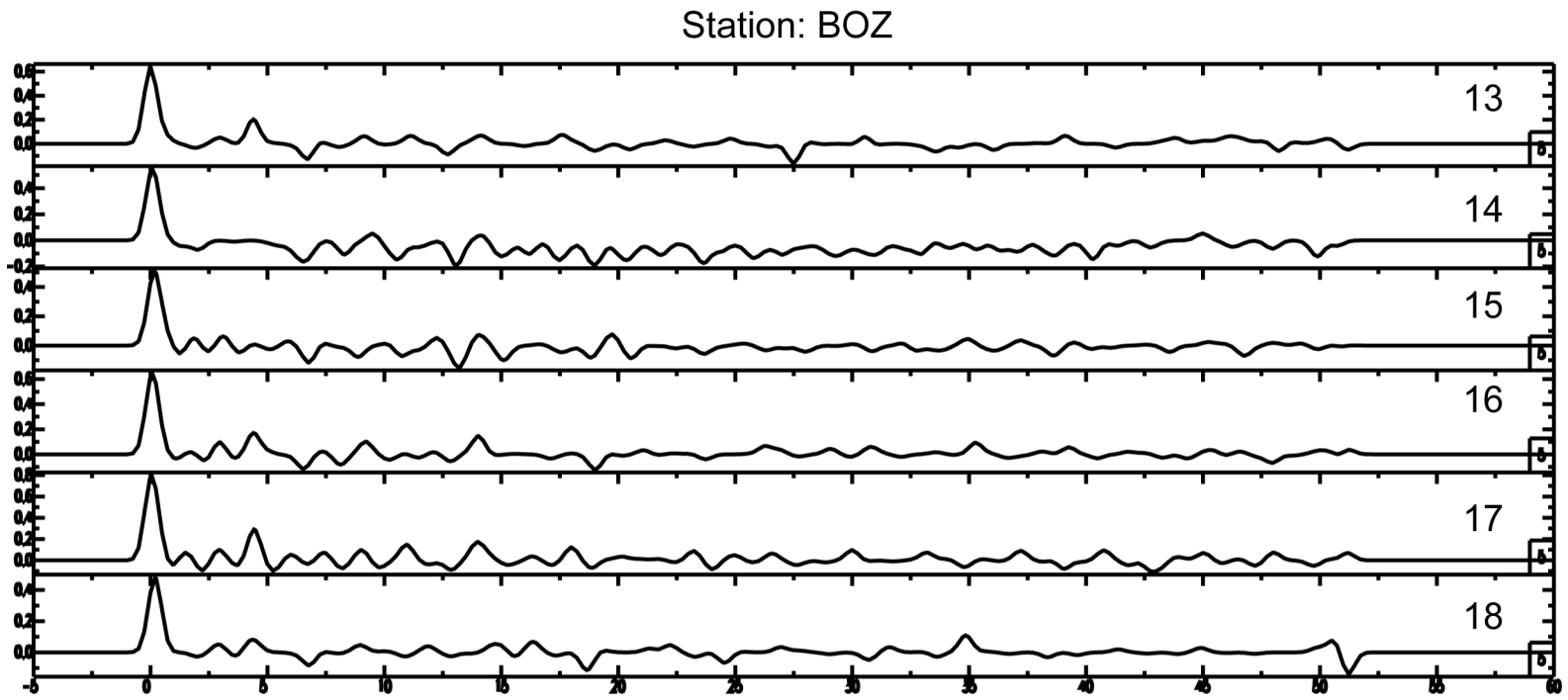


Figure 4-3. Six RFs for BOZ. X-axis is time (s), starting at 0 with the initial *P*-wave arrival, while the Y-axis is ground displacement. Julian Days and BAZ for the events are as follows: 13. 05288, 308.58; 14. 07197, 309.62; 15. 07197, 311.31; 16. 08187, 315.73; 17. 06142, 319.32; 18. 08133, 330.26.

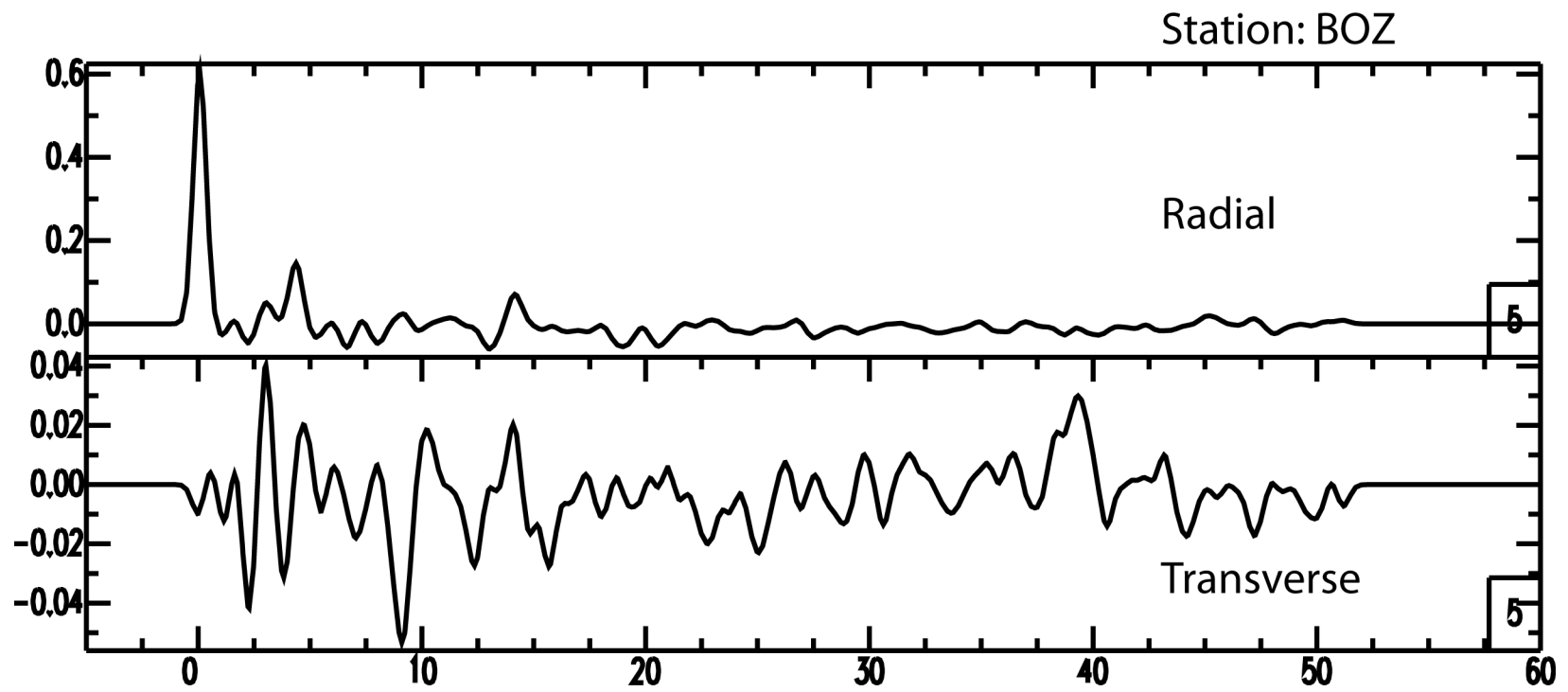


Figure 4-4. Radial and transverse RF stacks for BOZ. The radial stack includes the previous 18 receiver functions from 4-1 through 4-3.

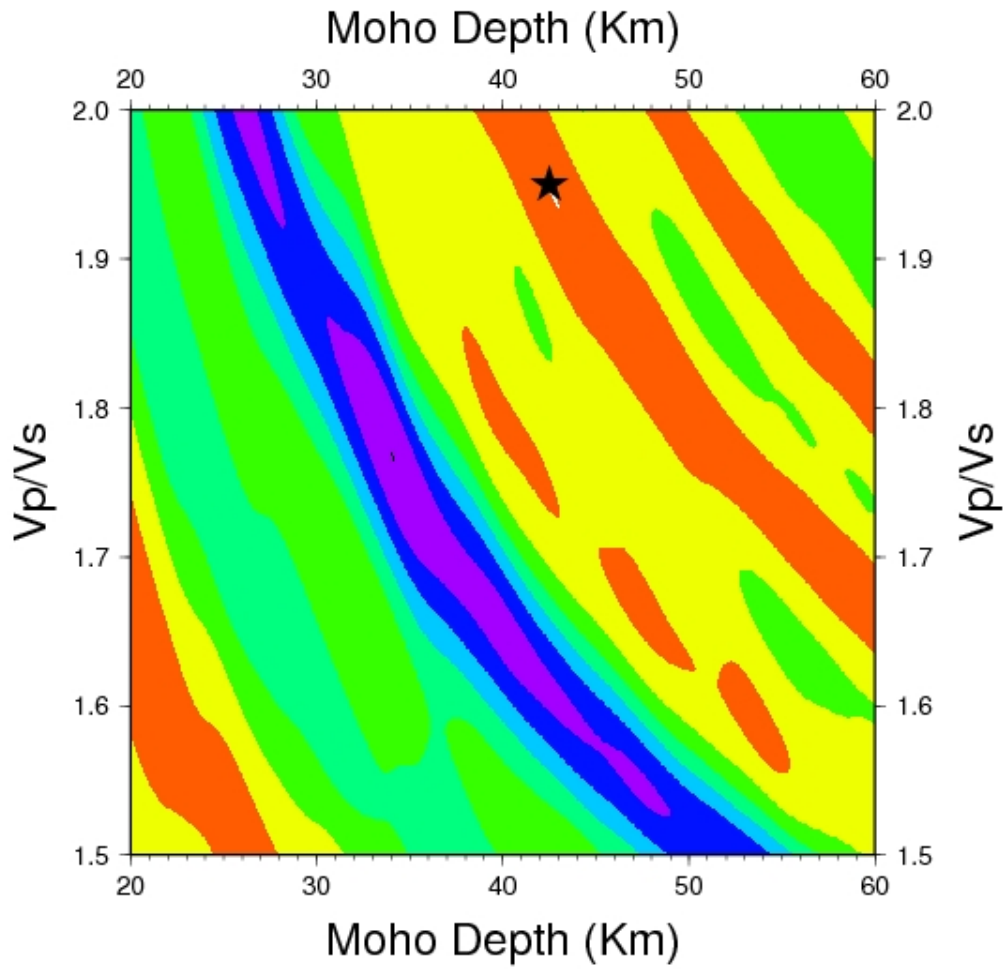


Figure 4-5. Stacking results for BOZ using the $s(H,\kappa)$ equation described in 2.3. The star represents the values of crustal thickness and V_p/V_s ratio that maximize the equation. $H = 42.5$ km, $\kappa = 1.95$.

Table 4-1. Location of seismometers, number of events used for each stack and resulting crustal thicknesses and Vp/Vs ratios.

Station	Latitude (N)	Longitude (E)	Elevation (m)	No.	H, km	Vp/Vs
BOZ	45.65	-111.63	1590	18	42.5	1.95
DGMT	48.47	-104.20	650	21	40.0	1.66
EGMT	48.02	-109.75	1060	4	52.0	1.94
EGMT	48.02	-109.75	1060	5	29.5	1.59
LAO	46.69	-106.22	900	21	38.0	1.62
MSO	46.83	-113.94	1260	9	45.5	1.97

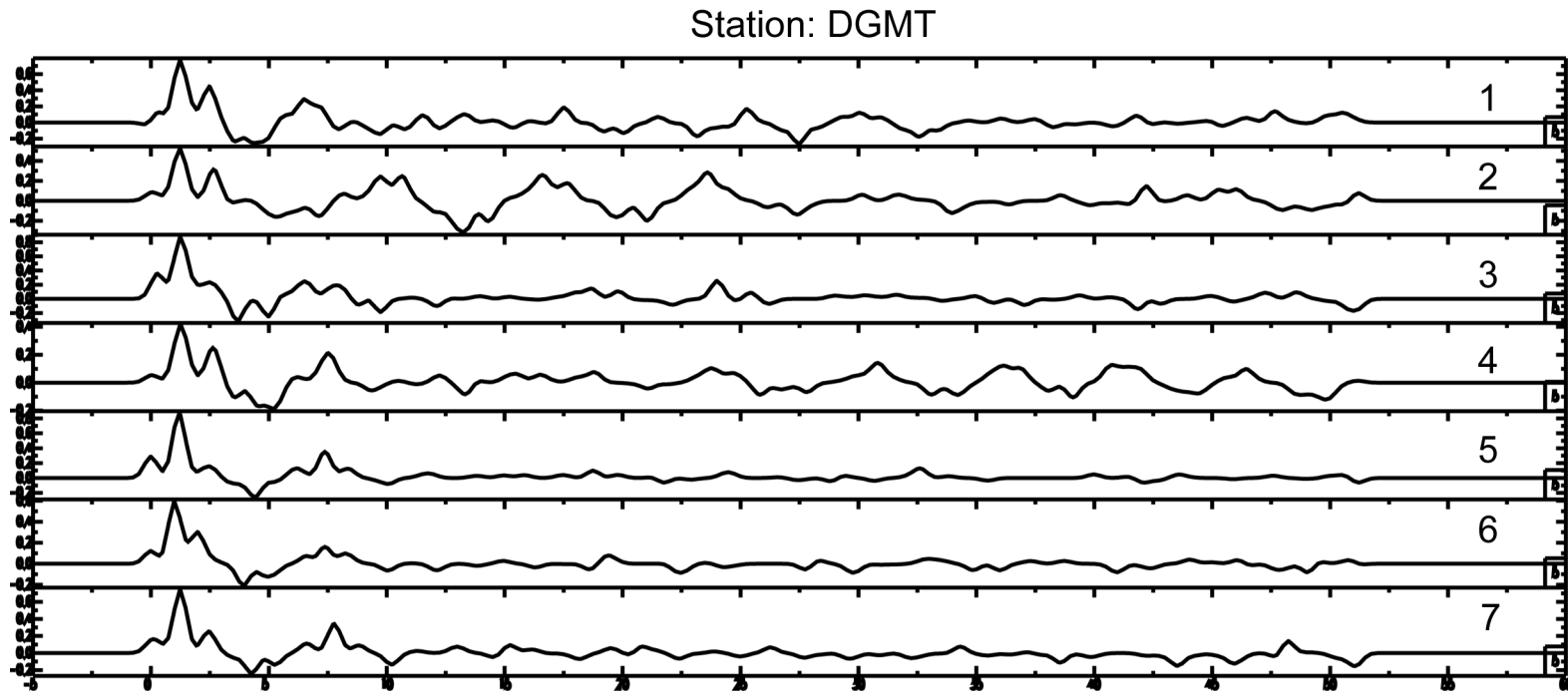


Figure 4-6. Seven RFs for DGMT. X-axis is time (s), starting at 0 with the initial *P*-wave arrival, while the Y-axis is ground displacement. Julian Days and BAZ for the events are as follows: 1. 08150, 38.09; 2. 07043, 62.15; 3. 07095, 69.45; 4. 07184, 101.66; 5. 04320, 143.75; 6. 05269, 147.29; 7. 07320, 147.45.

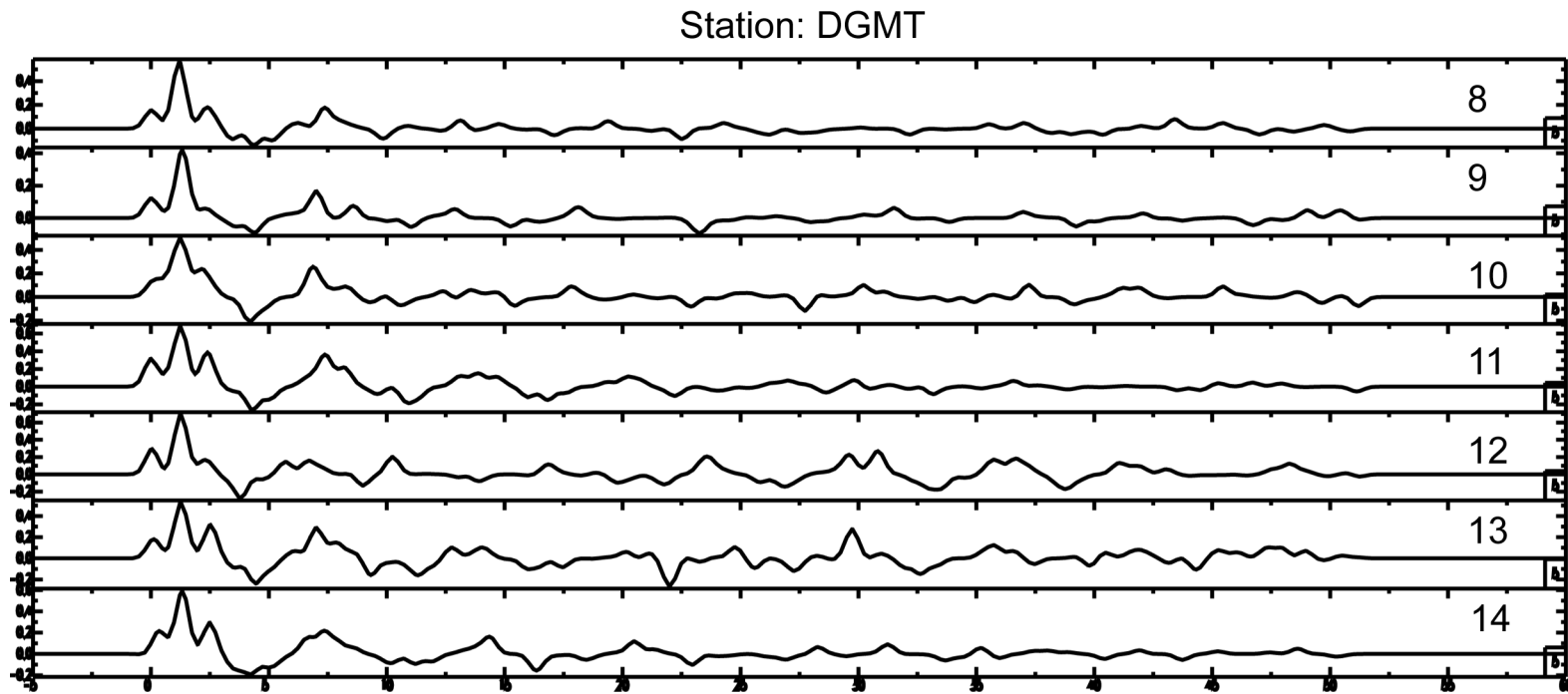


Figure 4-7. Seven RFs for DGMT. X-axis is time (s), starting at 0 with the initial *P*-wave arrival, while the Y-axis is ground displacement. Julian Days and BAZ for the events are as follows: 8. 07318, 147.57; 9. 07343, 240.74; 10. 06288, 254.14; 11. 08123, 303.24; 12. 07353, 303.40; 13. 07119, 304.37; 14. 07013, 310.46.

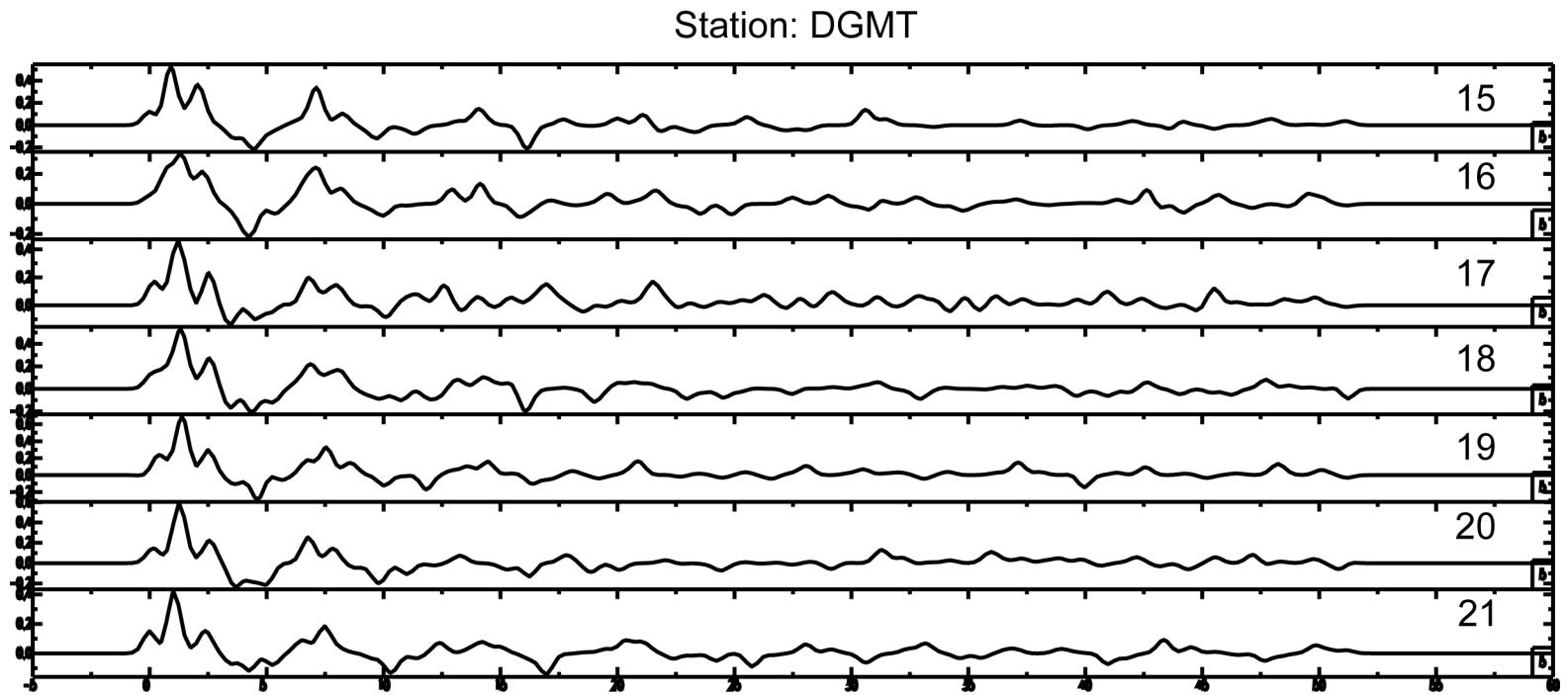


Figure 4-8. Seven RFs for DGMT. X-axis is time (s), starting at 0 with the initial *P*-wave arrival, while the Y-axis is ground displacement. Julian Days and BAZ for the events are as follows: 15. 06319, 311.41; 16. 07197, 313.77; 17. 07197, 315.69; 18. 08187, 317.69; 19. 06110, 319.57; 20. 08175, 334.60; 21. 08133, 336.43.

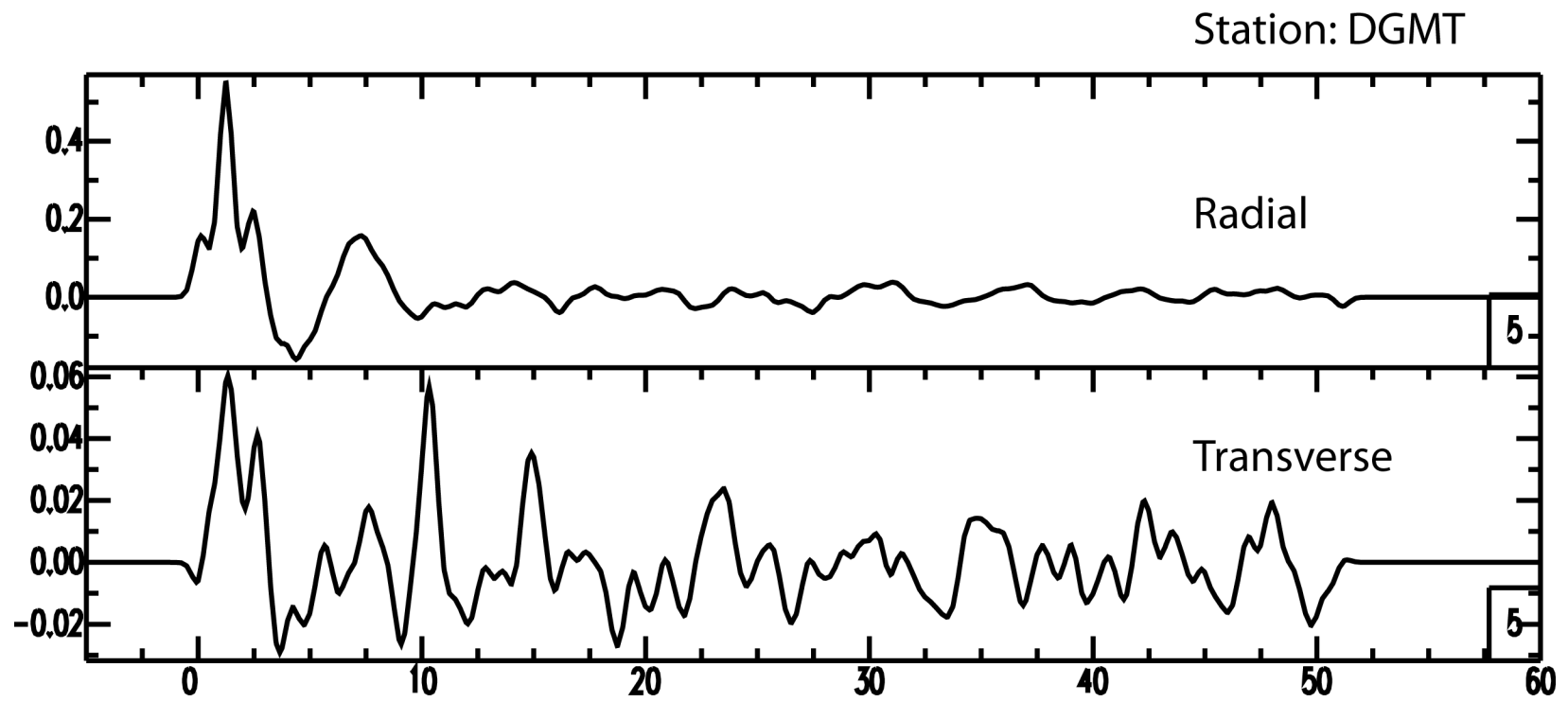


Figure 4-9. Radial and transverse RF stacks for DGMT. The radial stack includes the previous 21 receiver functions from 4-6 through 4-8.

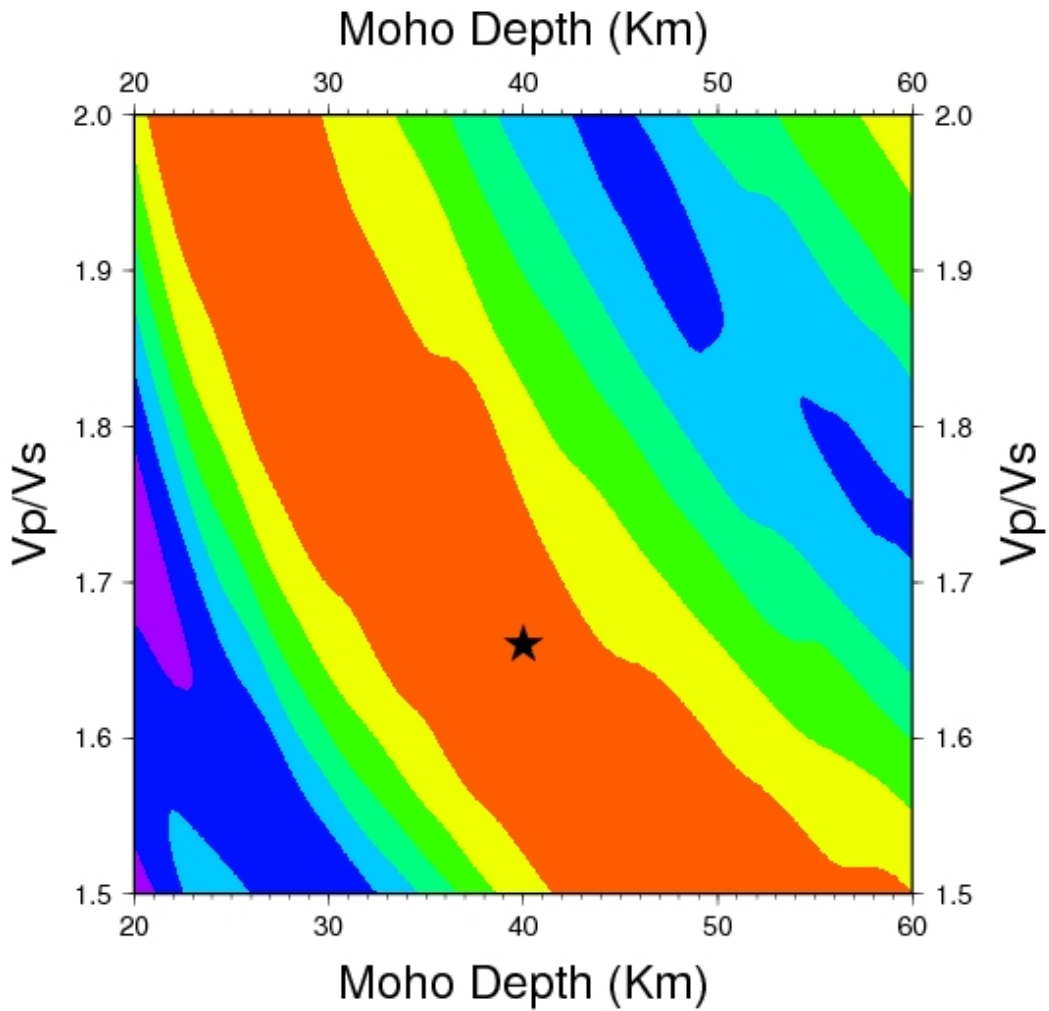


Figure 4-10. Stacking results for DGMT using the $s(H,\kappa)$ equation described in 2.3. The star represents the values of crustal thickness and Vp/Vs ratio that maximize the equation. $H = 40$ km, $\kappa = 1.66$.

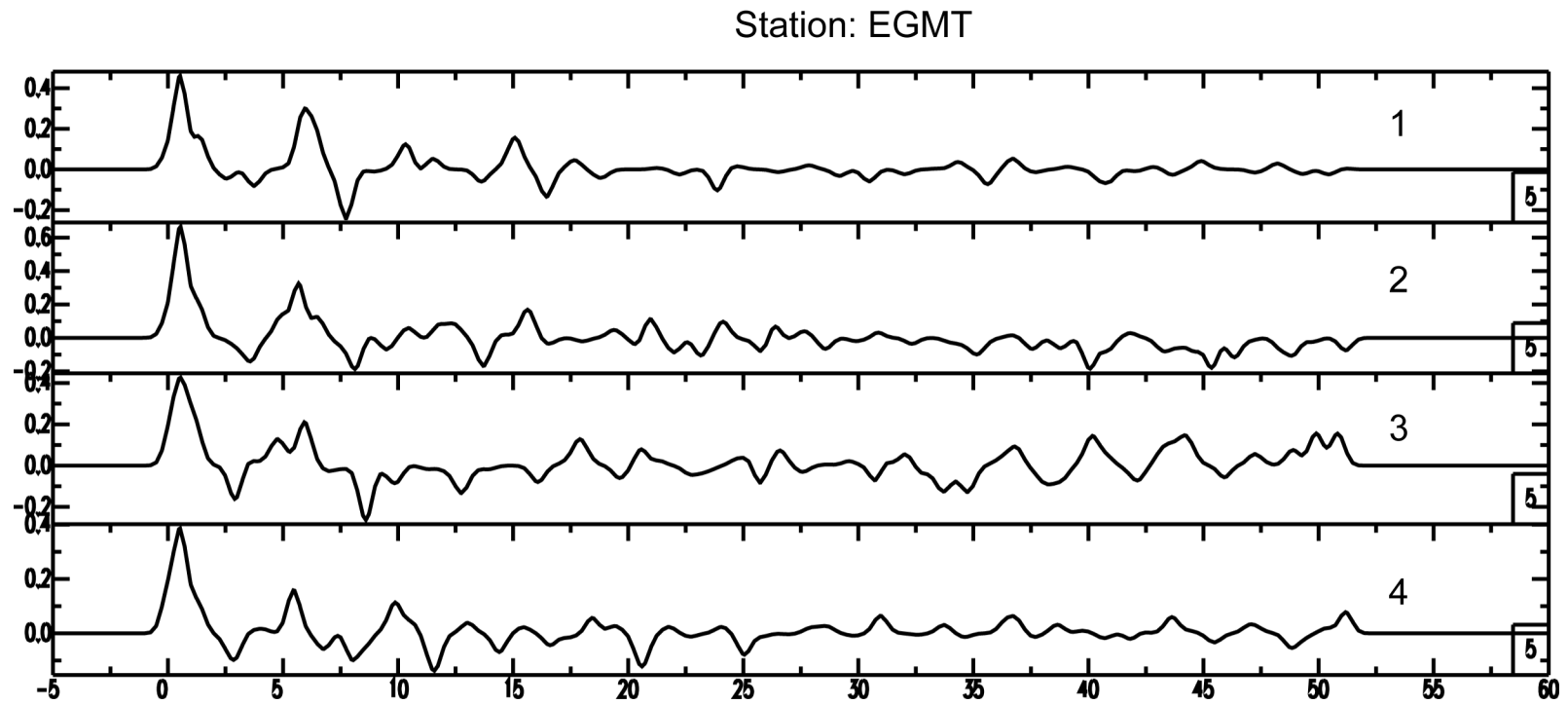


Figure 4-11. Four radial RFs for EGMT. X-axis is time (s), starting at 0 with the initial *P*-wave arrival, while the Y-axis is ground displacement. Julian Days and BAZ for the events are as follows: 1. 08150, 36.50; 2. 07043, 58.59; 3. 07095, 65.92; 4. 08133, 331.89.

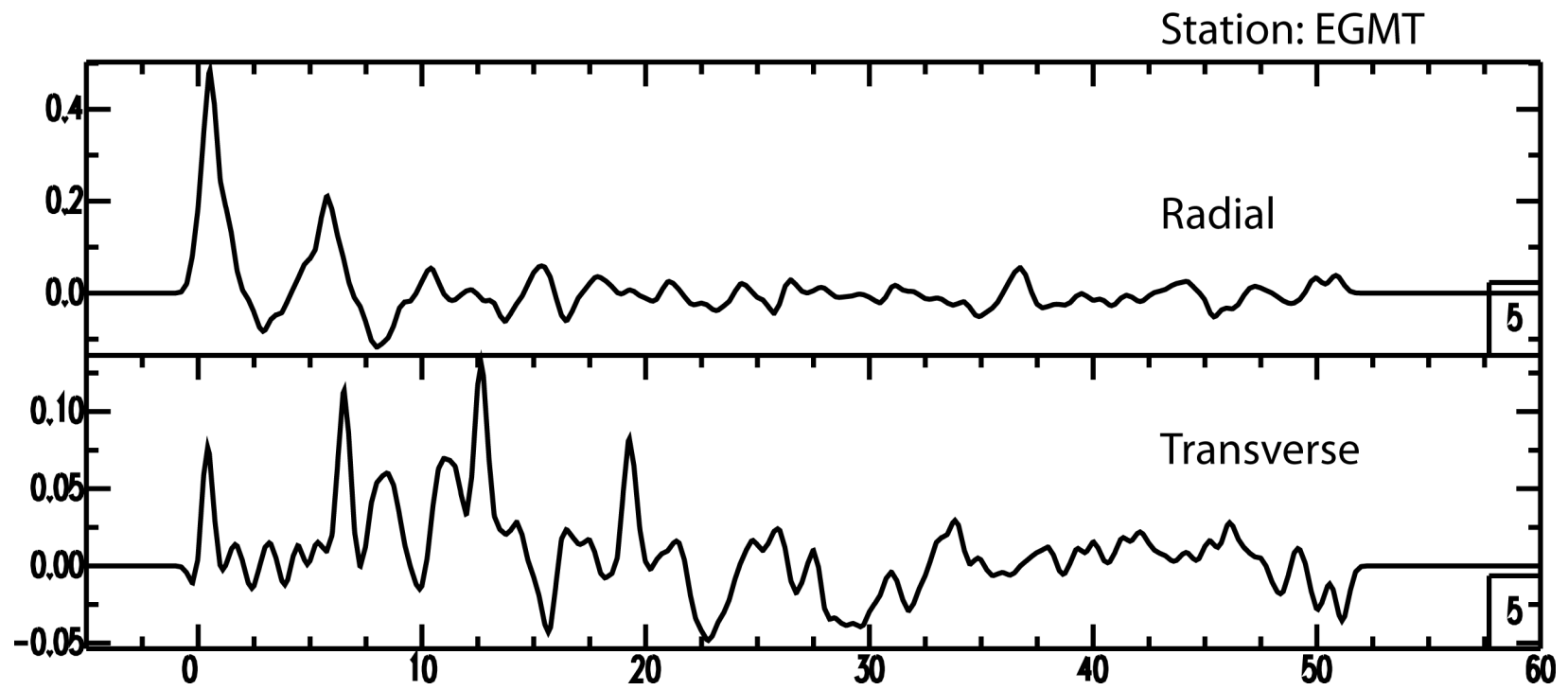


Figure 4-12. Radial and transverse RF stacks for EGMT. The radial stack includes the previous 4 receiver functions from 4-11.

Station: EGMT

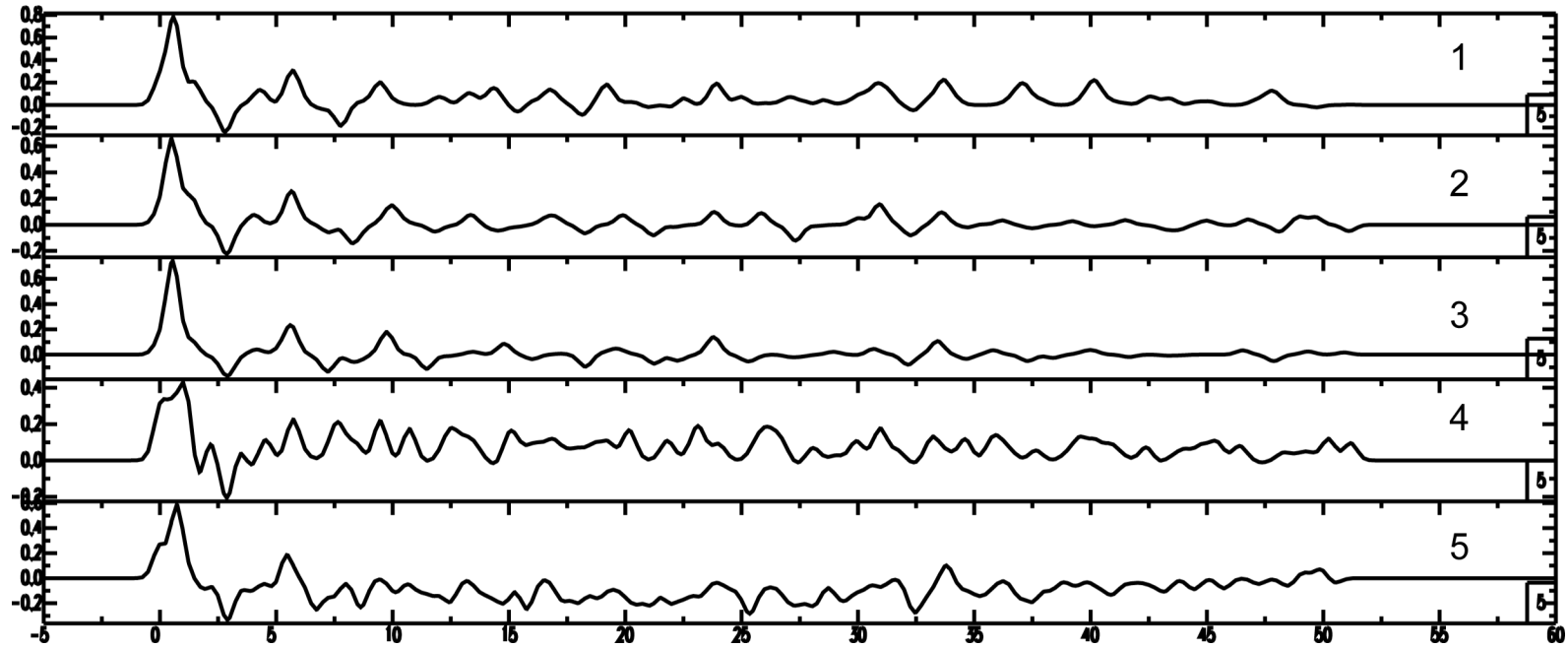


Figure 4-13. Five RF functions for EGMT. X-axis is time (s), starting at 0 with the initial *P*-wave arrival, while the Y-axis is ground displacement. Julian Days and BAZ for the events are as follows: 1. 08123, 301.57; 2. 07013, 307.74; 3. 06319, 308.69; 4. 07197, 312.12; 5. 08187, 315.43.

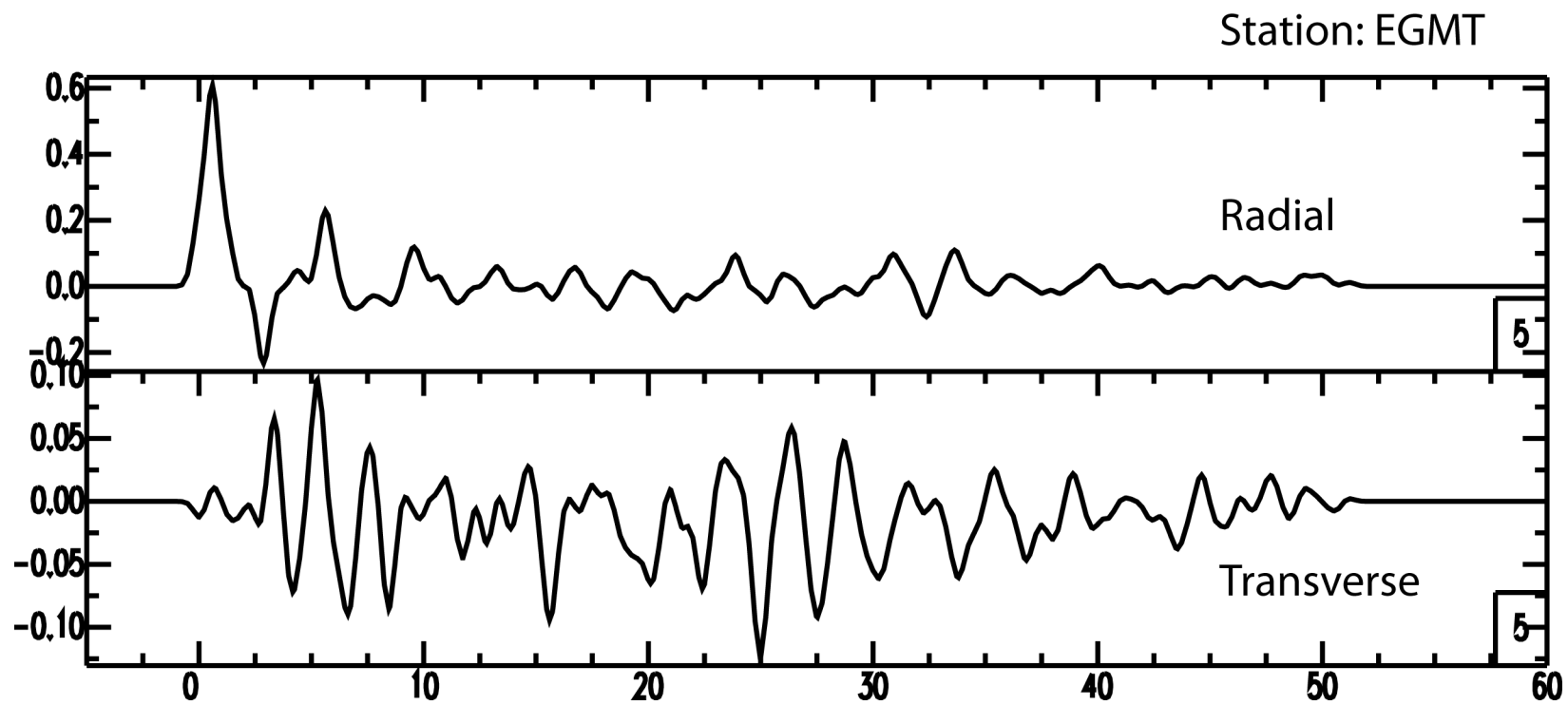


Figure 4-14. Radial and transverse RF stacks for EGMT. The radial stack includes the previous 5 receiver functions from 4-13.

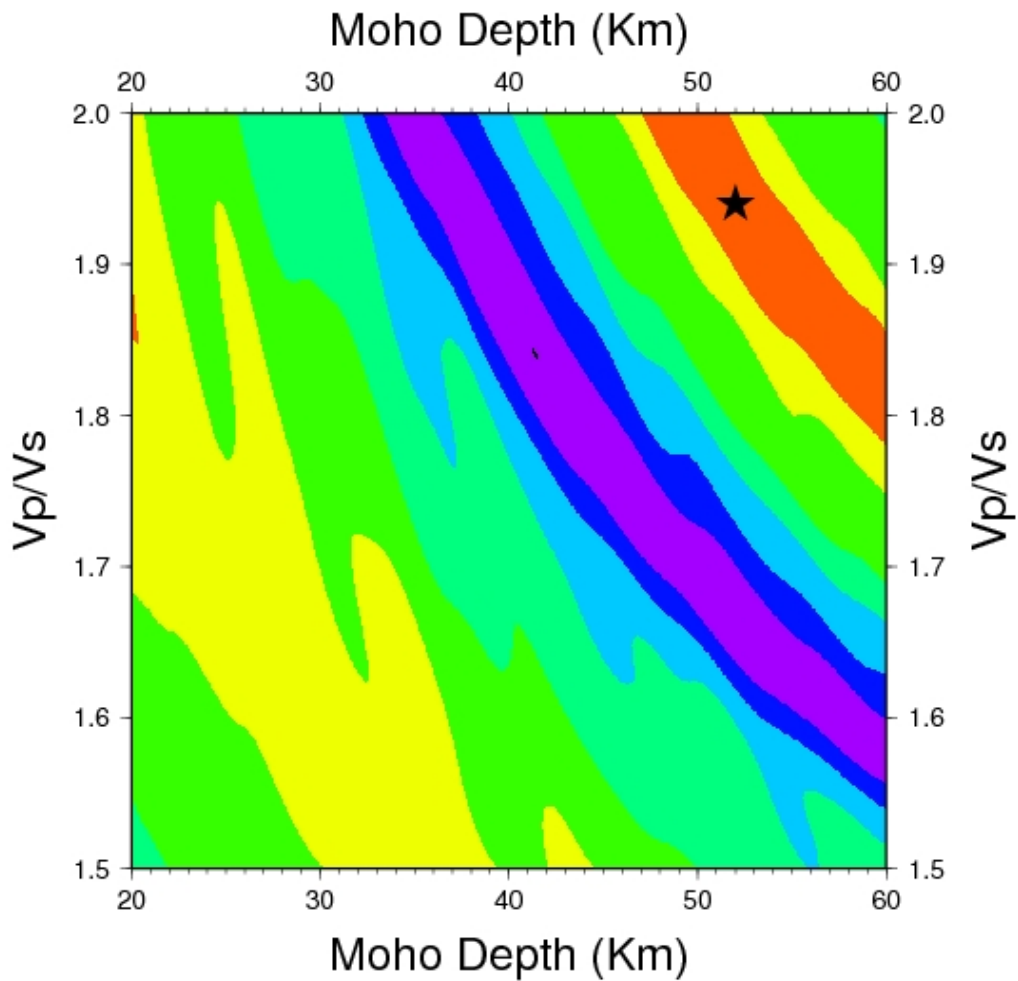


Figure 4-15. Stacking results for EGM T using the $s(H, \kappa)$ equation described in 2.3. The star represents the values of crustal thickness and V_p/V_s ratio that maximize the equation. This particular model for EGM T used 4 events with BAZ from the NE and NNW. $H = 52$ km, $\kappa = 1.94$.

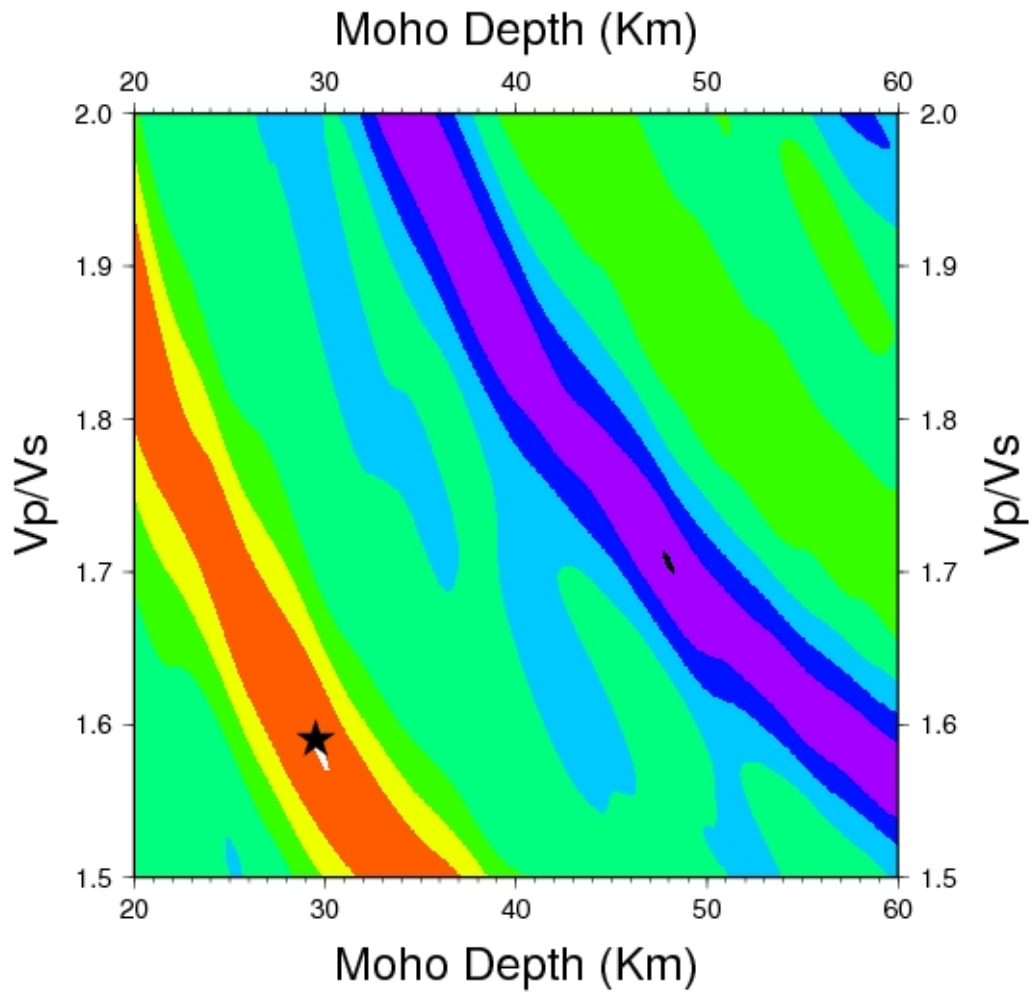


Figure 4-16. Stacking results for EGM T using the $s(H, \kappa)$ equation described in 2.3. The star represents the values of crustal thickness and Vp/Vs ratio that maximize the equation. This particular model for EGM T used 5 events with BAZ from the WNW. $H = 29.5$ km, $\kappa = 1.59$.

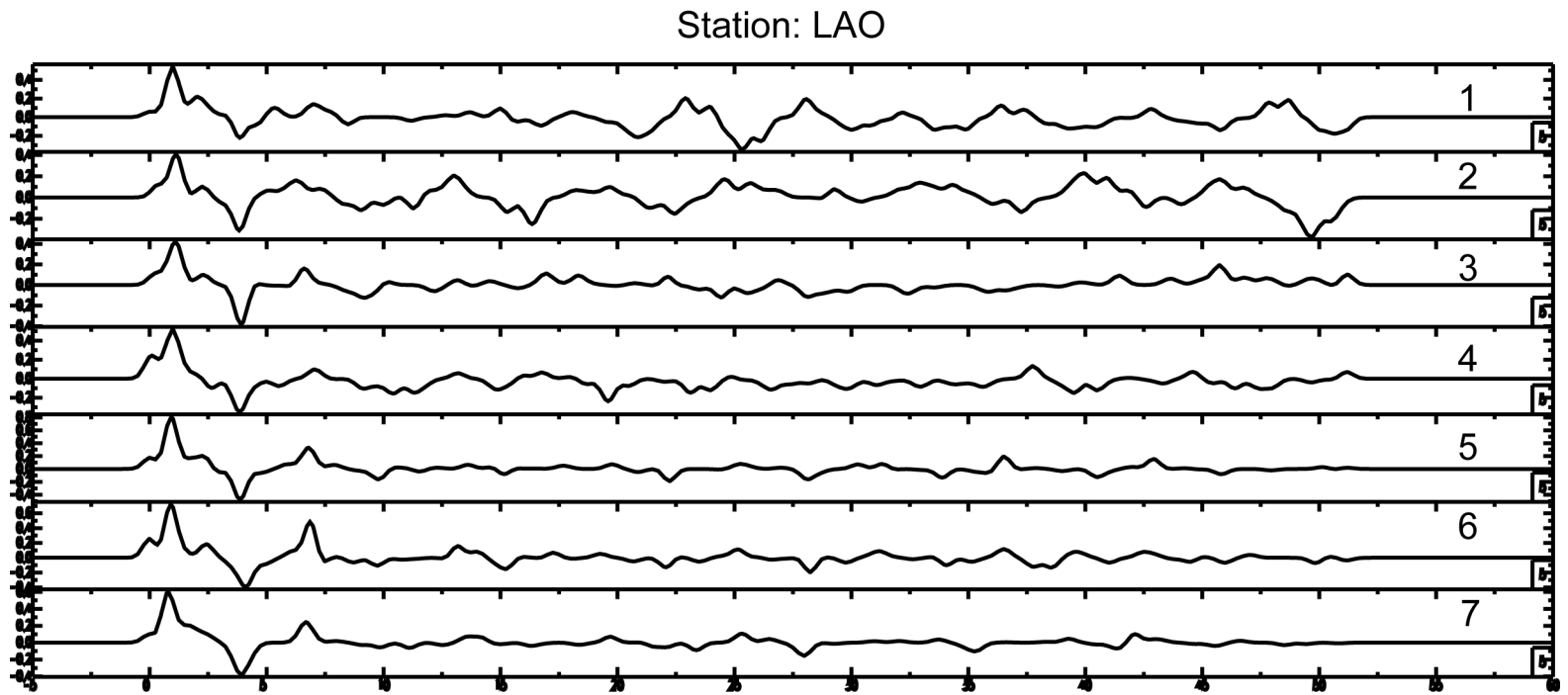


Figure 4-17. Seven RFs for LAO. X-axis is time (s), starting at 0 with the initial *P*-wave arrival, while the Y-axis is ground displacement. Julian Days and BAZ for the events are as follows: 1. 08150, 36.61; 2. 07043, 60.29; 3. 07095, 67.23; 4. 07184, 99.79; 5. 04320, 140.36; 6. 07320, 144.47; 7. 05269, 144.50.

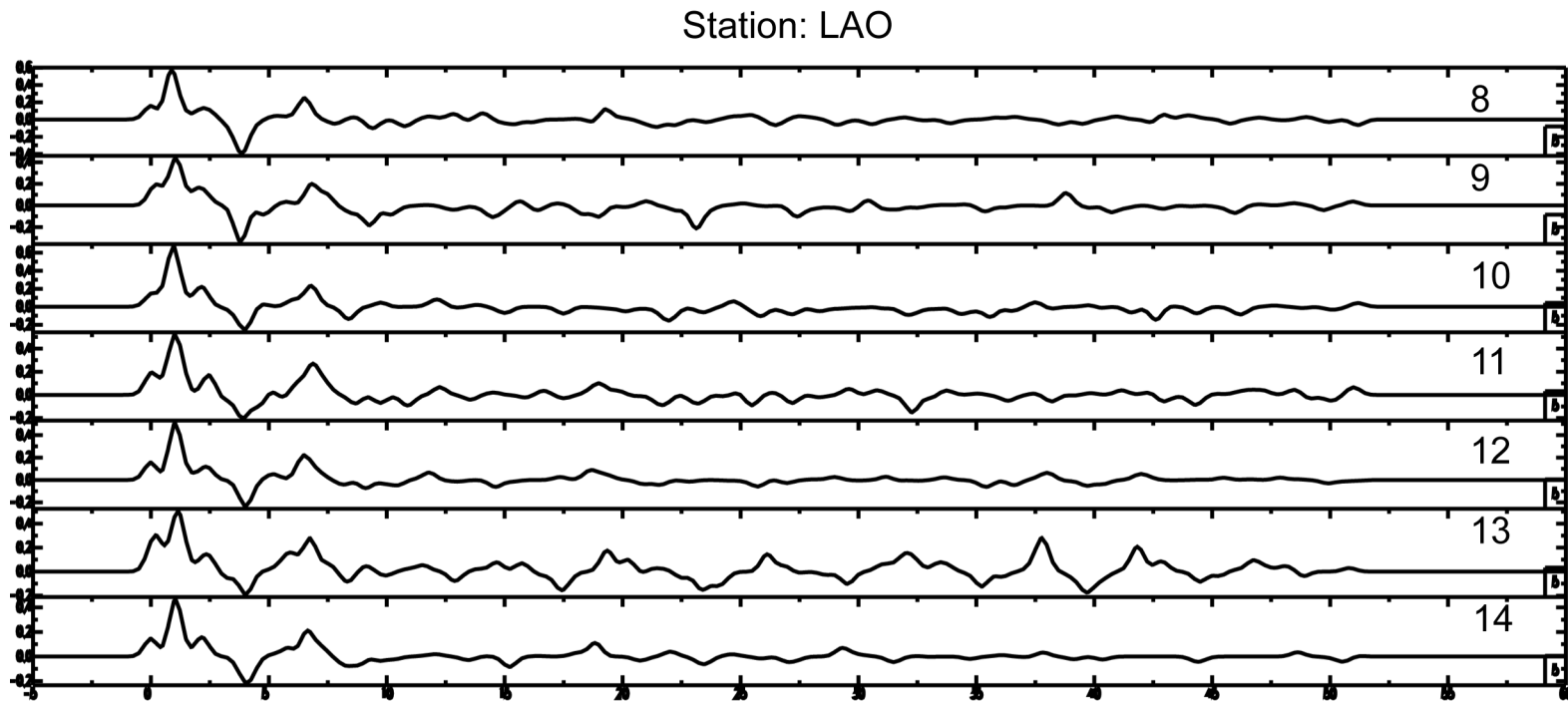


Figure 4-18. Seven RFs for LAO. X-axis is time (s), starting at 0 with the initial *P*-wave arrival, while the Y-axis is ground displacement. Julian Days and BAZ for the events are as follows: 8. 07318, 145.56; 9. 06288, 253.79; 10. 08123, 303.98; 11. 07119, 305.01; 12. 07013, 310.09; 13. 05288, 310.79; 14. 06319, 311.01.

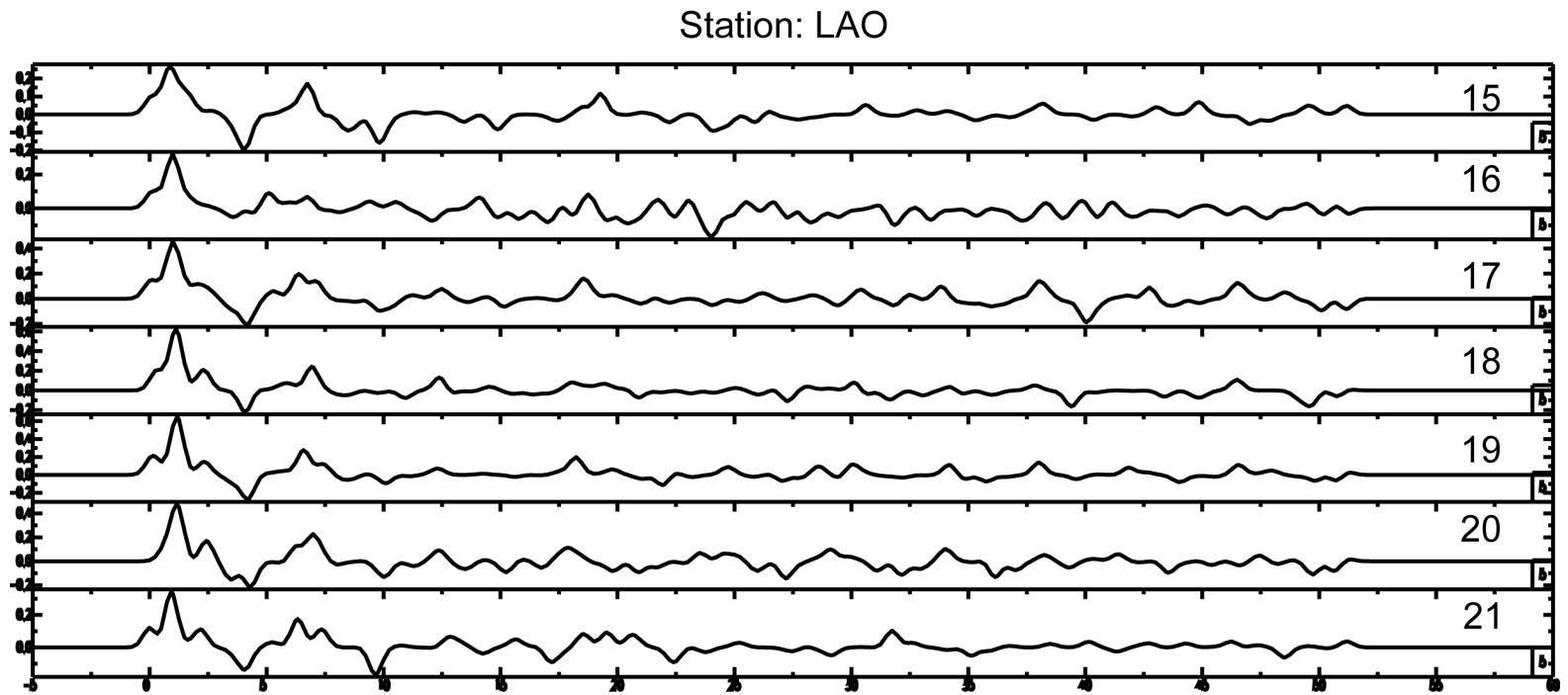


Figure 4-19. Seven RFs for LAO. Station X-axis is time (s), starting at 0 with the initial *P*-wave arrival, while the Y-axis is ground displacement. Julian Days and BAZ for the events are as follows: 15. 07197, 312.76; 16. 07197, 314.58; 17. 08187, 317.51; 18. 06119, 319.32; 19. 06110, 319.99; 20. 06142, 320.14; 21. 08133, 334.67.

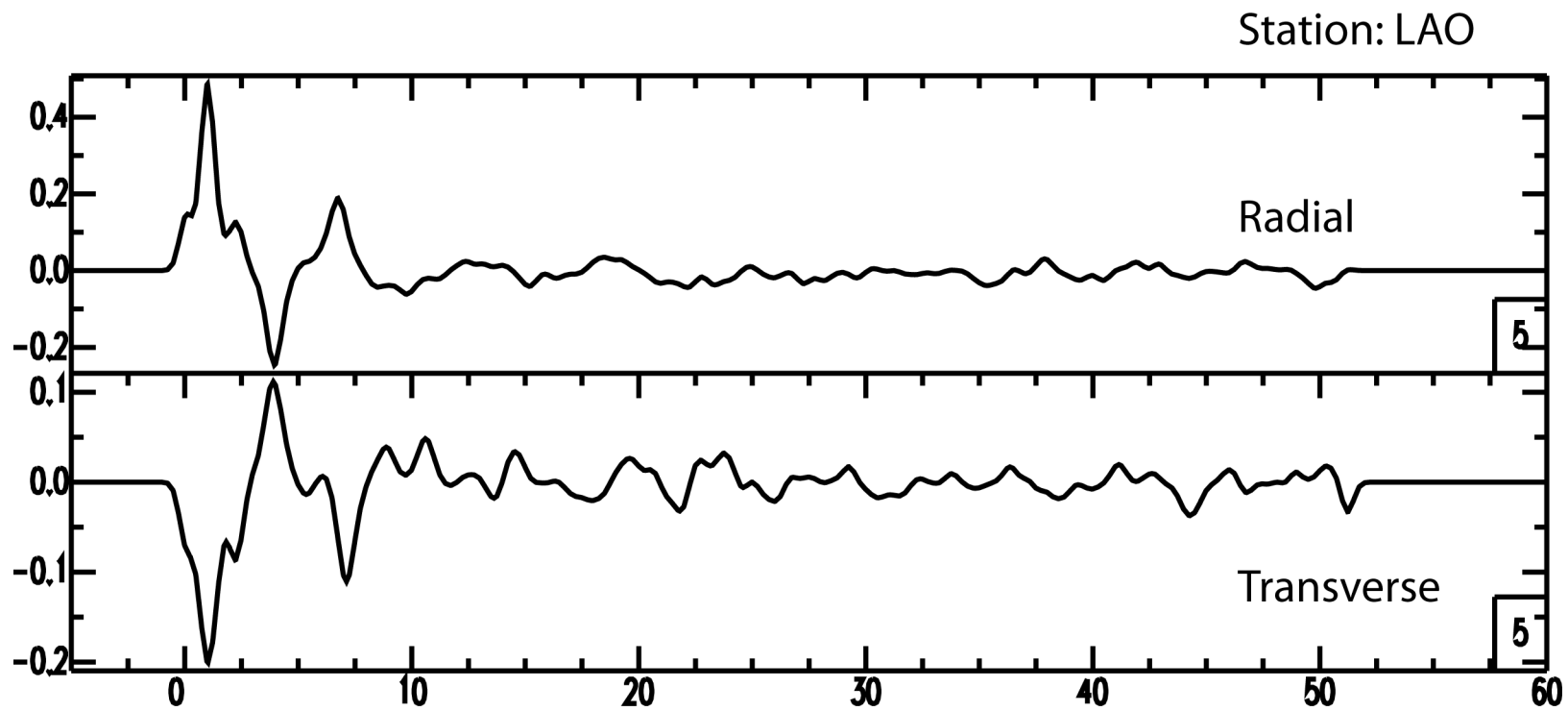


Figure 4-20. Radial and transverse RF stacks for LAO. The radial stack includes the previous 21 receiver functions from 4-17 through 4-19.

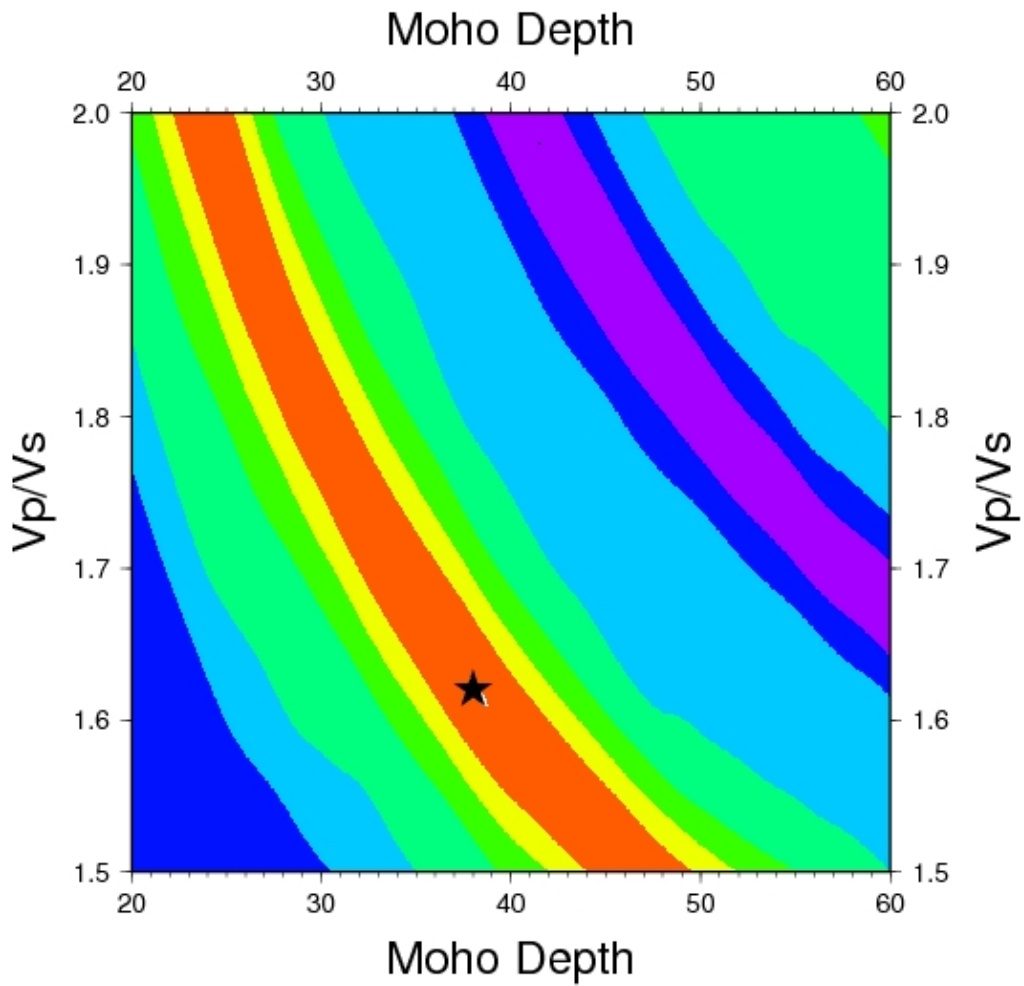


Figure 4-21. Stacking results for LAO using the $s(H,\kappa)$ equation described in 2.3. The star represents the values of crustal thickness and V_p/V_s ratio that maximize the equation. $H = 38$ km, $\kappa = 1.62$.

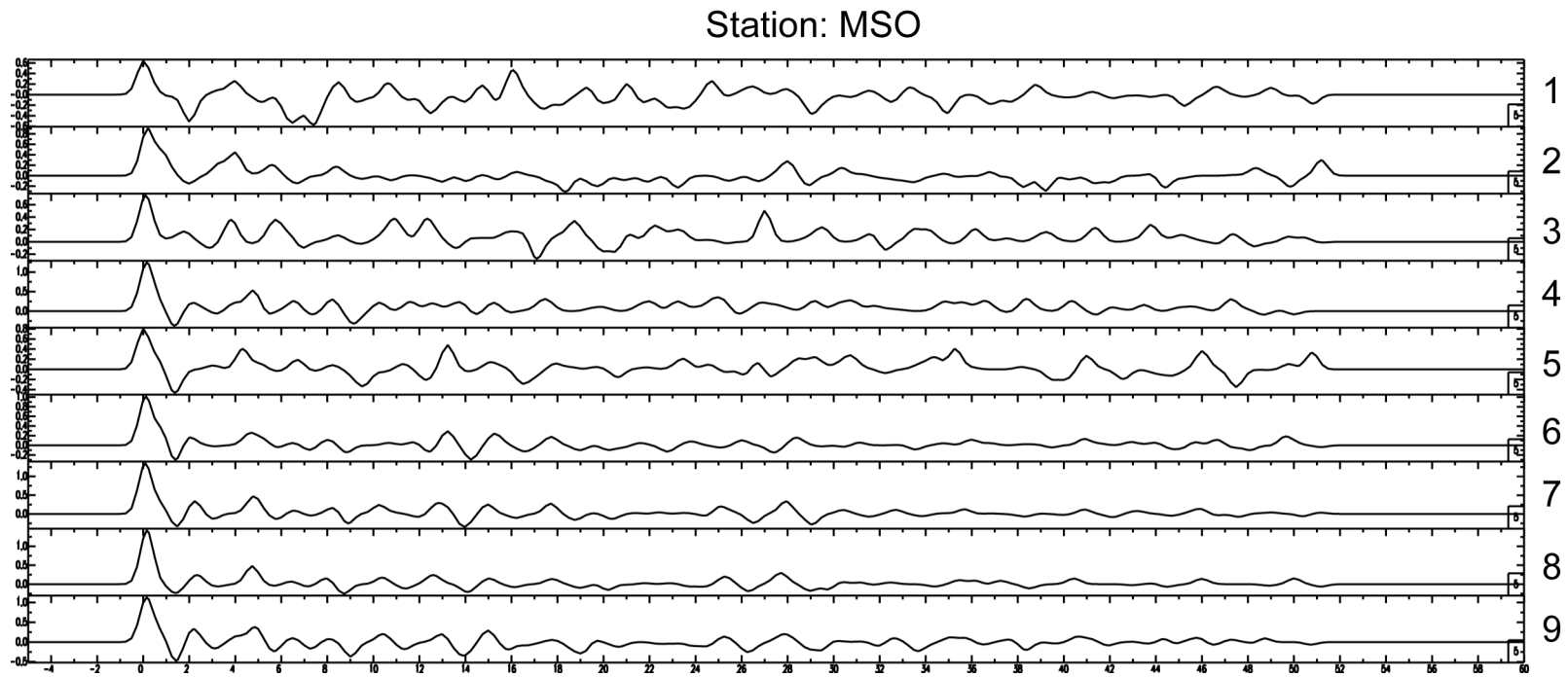


Figure 4-22. Nine RFs for MSO. Station X-axis is time (s), starting at 0 with the initial *P*-wave arrival, while the Y-axis is ground displacement. Julian Days and BAZ for the events are as follows: 1. 07043, 55.70; 2. 07095, 62.93; 3. 07184, 94.12; 4. 07119, 302.31; 5. 05288, 306.94; 6. 08187, 314.27; 7. 06119, 317.26; 8. 06110, 317.97; 9. 06142, 318.05.

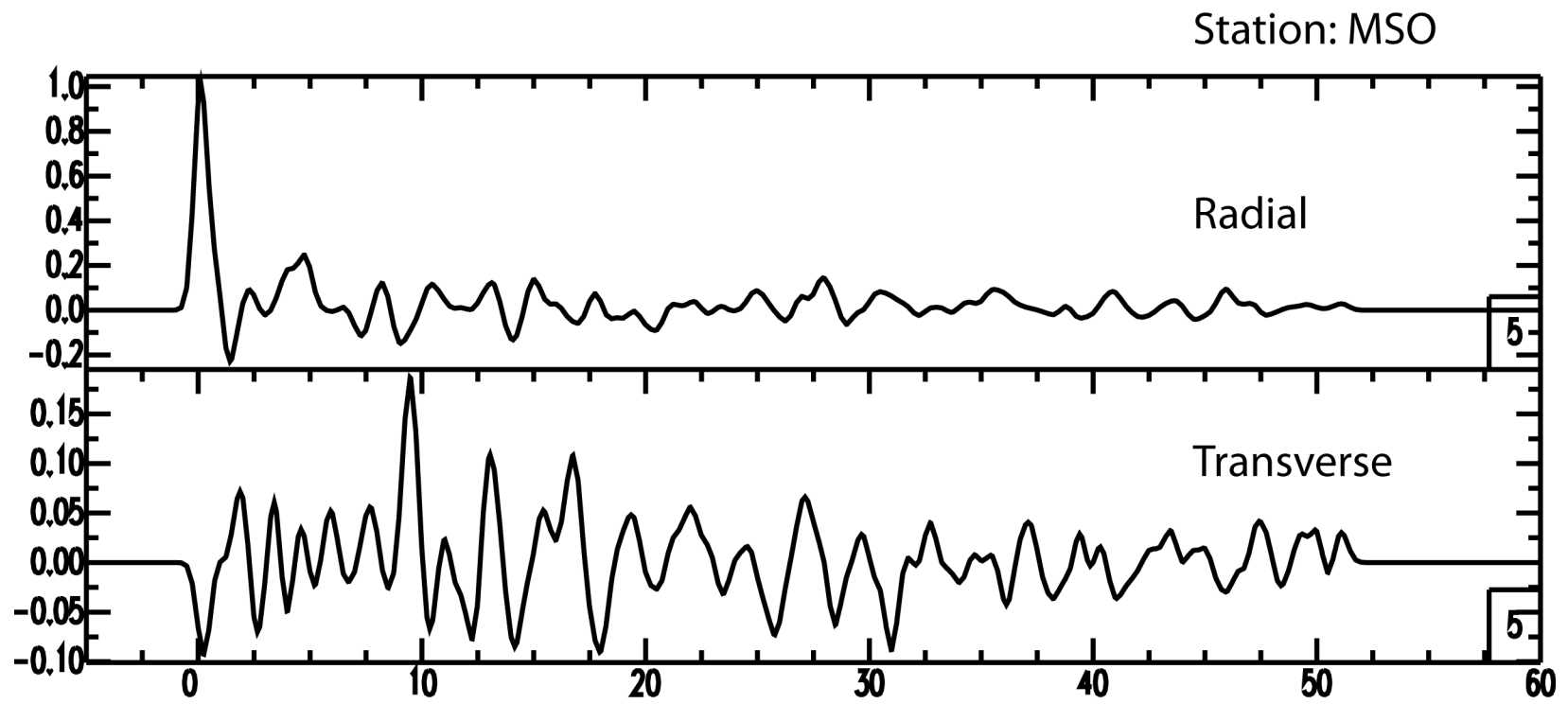


Figure 4-23. Radial and transverse RF stacks for MSO. The radial stack includes the previous 9 receiver functions from 4-22.

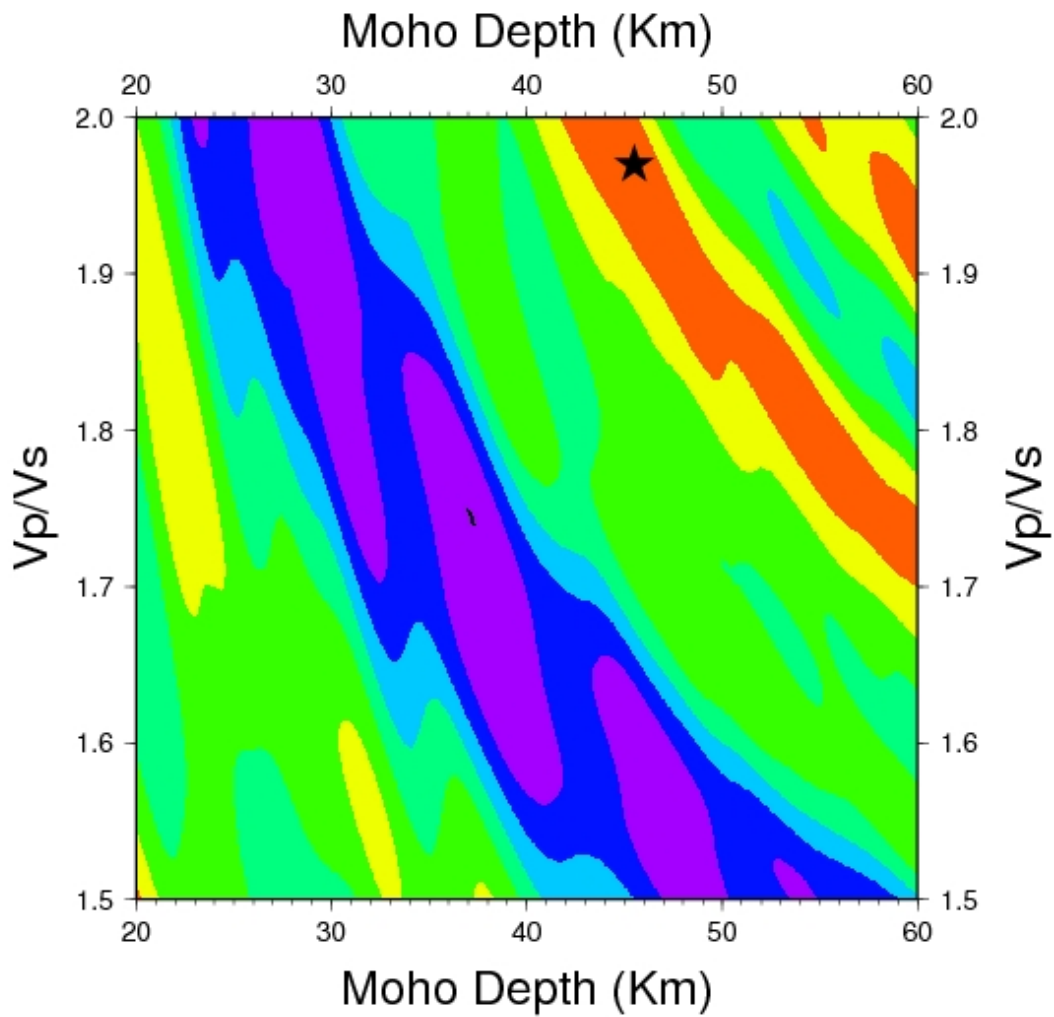


Figure 4-24. Stacking results for MSO using the $s(H,\kappa)$ equation described in 2.3. The star represents the values of crustal thickness and V_p/V_s ratio that maximize the equation. $H = 45.5$ km, $\kappa = 1.97$.

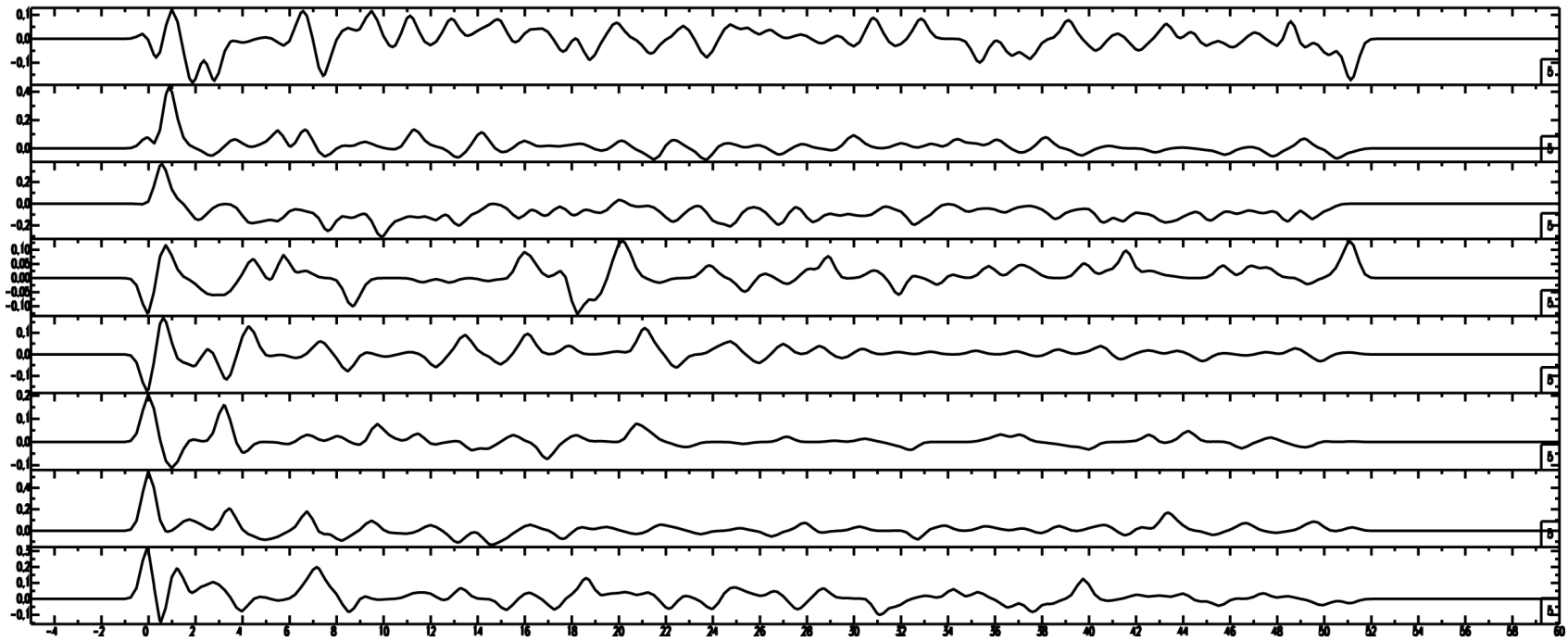


Figure 4-25. Eight radial RFs for RLMT. X-axis is time (s), starting at 0 with the initial *P*-wave arrival, while the Y-axis is ground displacement.

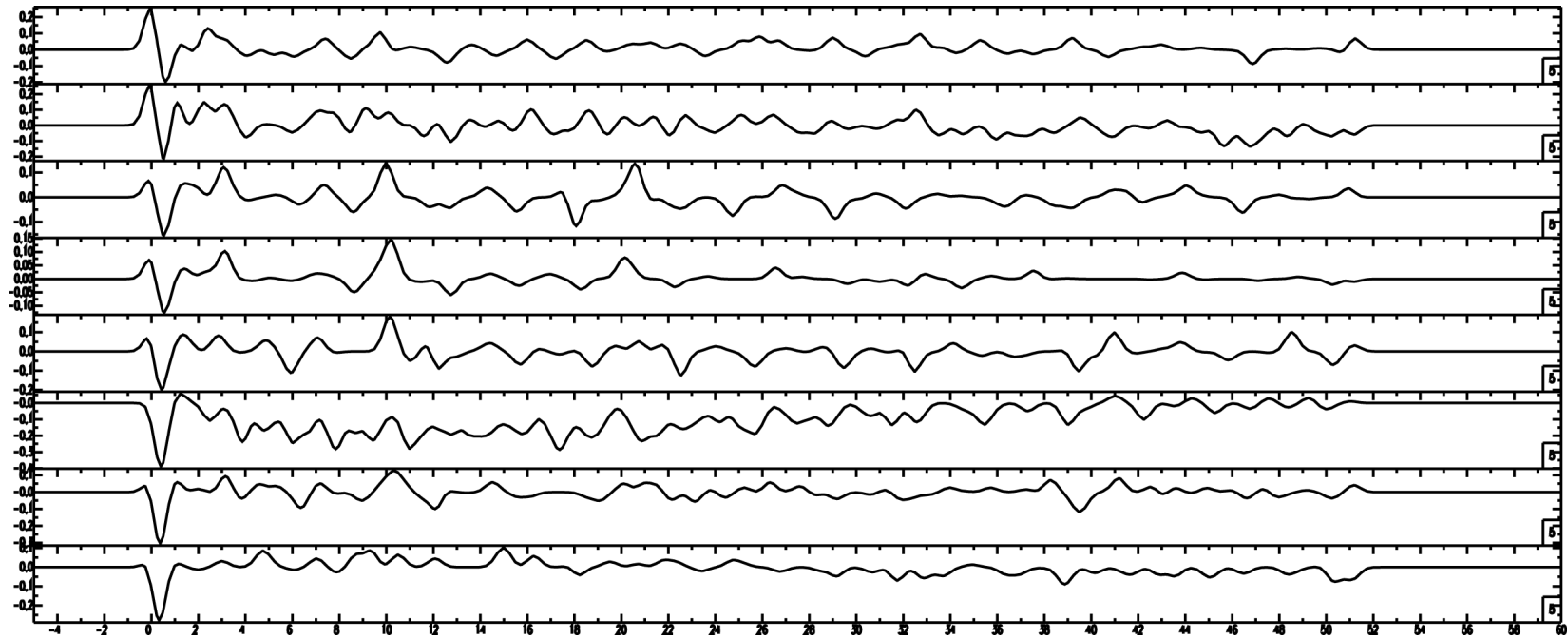


Figure 4-26. Eight radial RFs for RLMT. X-axis is time (s), starting at 0 with the initial *P*-wave arrival, while the Y-axis is ground displacement.

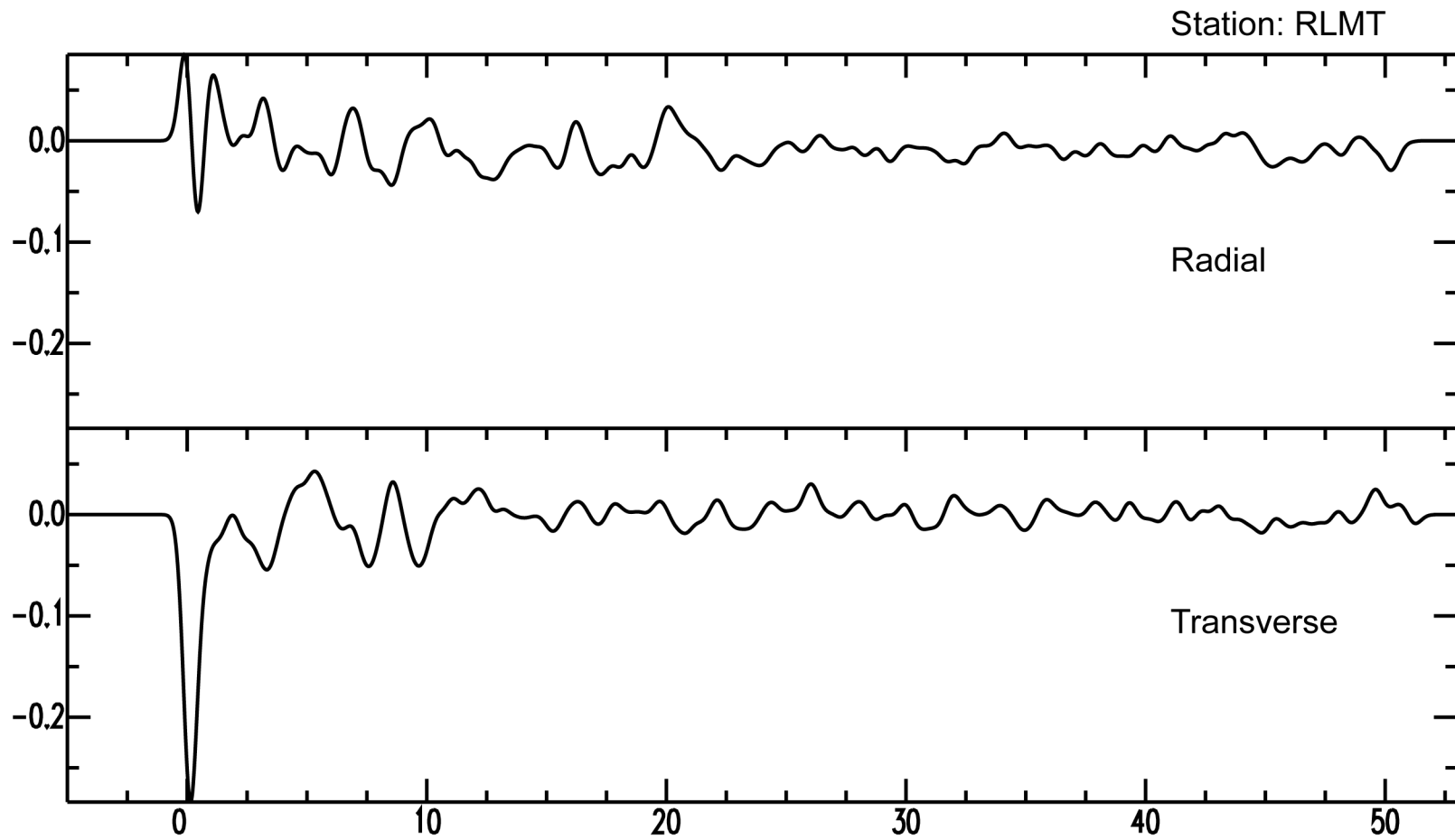


Figure 4-27. Radial and transverse RFs stacks for RLMT. The radial stack is comprised of the previous 16 RFs in Figure 4-25 and 4-26. The amplitude is diminished due to the lack of coherence in the individual RFs. The large negative amplitude in the transverse RF is indicative of a complex structure, likely a dipping layer or non horizontal Moho.

CHAPTER 5 DISCUSSION

5.1 Basin vs. Range

BOZ, MSO, DGMT, and LAO can be grouped into two distinctive groups. DGMT and LAO both exhibit scattered initial *P*-wave arrivals followed by strong negative amplitudes before the *Ps* arrival, have V_p/V_s ratios less than 1.7, and have crustal thicknesses of 40 km or less (Figures 4-9 and 4-20; Table 4-1). BOZ and MSO have strong *P* arrivals, a shorter time delay between *P* and *Ps*, lack the strong negative amplitude, display V_p/V_s ratios higher than 1.9, and have Moho depths greater than 40 km (Figures 4-4 and 4-23; Table 4-1). DGMT and LAO are located in the Williston Basin and BOZ and MSO are situated in the Northern Rocky Mountain belt (Figure 1-3). The distinction and differences between the two sets are not coincidences and can be attributed to their locations.

The anomalous initial *P* arrivals and negative amplitude associated with LAO and DGMT can be attributed to the basin sediments beneath each station. The velocity contrast between the Precambrian rock of the Trans-Hudson Orogen and the sediments of the Williston Basin explain the negative anomaly as well as the scattered *P* arrivals. Reverberations and various *P*-to-*S* conversions at the basin bottom (Baird et al., 1995) could cause multiple phases to arrive 1-2 seconds apart (Assumpção et al., 2002).

The basin stations are estimated to have thinner crust compared to that of the mountains due to the lack of crustal roots. Evidence for this comes from the North American gravity map showing large negative anomalies beneath the Northern Rockies and fading to the east into the basin (Tanner et al., 1988). However, these crustal

thickness values are not much lower than the Rocky Mountain stations. This is most likely a result of the amount of infill that has taken place since the Cambrian, when the basin began to subside (Leighton and Kolata, 1990). The crustal thicknesses for these stations are similar to a previous project done north of the US border that produced a value of 42 km (Baird et al., 1995). This COCRUST (Consortium for Crustal Reconnaissance Using Seismic Techniques) project used wide-angle reflection-refraction data to image the crust-mantle boundary.

5.2 EGMT

The Eagleton station represents an oddity in the study. Two different outputs, based on BAZ, display characteristics of both the aforementioned basin and mountain stations. The first stack, Figure 4-15, displays a thick crust with a high Vp/Vs ratio, similar to the mountain stations (BOZ, MSO). The second set for EGMT results in a thinner crust with a lower Vp/Vs ratio, closer to that of DGMT and LAO. EGMT is situated on the border of the GFTZ with the MHB. The GFTZ is a poorly understood structure sandwiched between the MHB and WC. It is likely a suture point for these two Archean cratons and thus has a complex structure including folds, faults and dipping layers (Mueller et al., 2002). Incoming P-to-S conversions are likely affected by these high strained structures producing variable RFs depending on the BAZ (NE-NNW or WNW). Figure 5-1 provides an example of the structure beneath EGMT. To the north of the station where shot spacing and resolution are better, layers are folded and there is a step-down in the Moho and LCL. These various features are all plausible explanations for the two different EGMT outputs.

5.3 Vp/Vs

Holbrook et al. (1992) computed Vp/Vs ratios for multiple crystalline basement compositions. Their results show higher Vp/Vs ratios for mafic rocks (>1.8), and lower ratios for felsic rocks (< 1.8). If we assume that the entire Wyoming craton is represented by a single crystalline layer, then we can only attribute the changing Vp/Vs ratios to the basin cover; however, the Williston Basin strata should have a higher Vp/Vs ratio according to Brauer et al. (2007). The Vp/Vs ratio for such sediments should be > 2 in most cases. With such low κ values, (~ 1.65) it is more likely that these basin stations are dominated by a silica-rich crystalline basement that is relatively unaffected by the 2000-3500 m thick Williston Basin strata.

If this is the case, then why do BOZ and MSO have such high κ values? Gorman et al. (2002) proposed a LCL with relatively fast P-wave velocities and attributed this to a mafic magmatic underplating event. Using the two xenoliths from Ross (2002), Gorman et al. (2002) postulated the emplacement to have taken place during the Proterozoic. Adopting this hypothesis, it would be reasonable to assume an underplating event occurred beneath MSO and BOZ. This idea is based on work by Tomlinson et al. (2006), that shows increased Vp/Vs ratios for underplating events. Based on this, I do not believe the LCL extends to the east beneath DGMT and LAO. The structures beneath RLMT and EGMT are too complicated to say with confidence whether or not the LCL exists at these locations.

5.4 Previous Publications

The Crust 2.0 model and Earthscope Automated Receiver Survey (EARS) have estimated crustal thickness for the seismic sites in this survey. The Crust 2.0 model

used 360 1-D seismic profiles and assigned each to a 2 x 2 degree (latitude and longitude) cell using surface wave tomography. Each depth profile includes 7 layers: ice, water, soft sediments, hard sediments, upper crust, middle crust, and lower crust. V_p , V_s and density are assigned for each layer (Basin et al., 2000). The EARS used similar techniques to this study, but due to the fact that it was automated, erroneous data sets may have been included within the processing. These errors include data gaps and low signal-to-noise ratios. The automated survey also included events greater than 90° from the station and magnitudes less than 6 (Crotwell and Owens, 2005).

The results for these studies vary; however, some are similar to the results of this project. Results for BOZ are as follows: Thesis – 42.5 km, Crust 2.0 – 43 km, EARS – 35 km. DGMT: Thesis – 40 km, Crust 2.0 – 48 km, EARS – 47 km. EGMT: Thesis – 52 and 29.5 km, Core 2.0 – 48 km, EARS – 39 km. LAO: Thesis – 38 km, Core 2.0 – 48 km, EARS – 43 km. MSO: Thesis – 45.5 km, Core 2.0 – 38 km, EARS – 50 km (Basin et al., 2000; Crotwell and Owens 2005). The stations located in the Northern Rocky belt (BOZ and MSO) generally agree with the Core 2.0 study, while the basin stations are more similar to those of the EARS study. One possible connection with the basin stations and EARS is the fundamental idea behind radial RFs. Radial RFs are used to image horizontal layers and undulations, similar to those on the Canadian side of the Deep Probe-SAREX experiments, may produce multiple radial RF responses and ultimately different resulting values for crustal thicknesses.

A COCORP seismic reflection study by Latham et al. (1988) traversed north-central to north-eastern Montana and can be compared with results from DGMT and EGMT. In north-central Montana, seismic reflections cease at ~15 secs two-way travel

time (TWTT), equivalent to a ~48 km depth for the Moho. The reflection results vary depending on arrival direction to the receiver, similar to our results for EGMT. A crustal thickness of 48 km compares well with the 52 km result we obtained for EGMT1. In north-eastern Montana the reflection results indicate the crust to be 39-45 km thick, similar to the 40 km crustal thickness we derive beneath DGMT. Latham et al. (1988) also saw evidence for a high velocity layer beneath this region; however, the velocities peak around 7.1 km/sec and are not as high as the 7.5 or higher velocities associated with the Deep Probe-SAREX line. Discrepancies within the velocity models of the two studies account for the different maximum velocities.

Sheriff and Stickney (1984) collected seismic refraction data from two open pit mine blasts in 1982. The receiver line extended 250 km NE-SW between Butte, Montana and Challis, Idaho with a station spacing of ~25 km. This line lies between stations BOZ and MSO, and, nominally, the refraction results can be compared with our results at those stations. However, the average crustal thickness found for the refraction study was ~33 km, with little variation along the line, assuming an average *P* velocity of 5.9 km/sec, and neglecting obvious crustal heterogeneities along the section profile. Clearly, this refraction line traverses a heterogeneous crust unlikely to be unvarying in thickness. It is similarly unlikely that the crustal heterogeneities can be safely neglected in a reflection study, even if station spacing is very wide, as in the Sheriff and Stickney (1984) study, and finally, the crustal *P* wave velocity assumed by the authors is more than 0.5 km/sec slower than the average for continental crust, so we consider these results suspect. A higher – more appropriate – mean crustal *P* wave velocity in the refraction modeling would increase the estimate of crustal thickness, leading to a Moho

depth more consistent with my RF results of 42.5-45.5 km for BOZ and MSO.

Furthermore, if the LCL does underlie the area around BOZ and MSO, the refraction study could very well have imaged the top of the LCL rather than the crust-mantle transition, which lies at similar depths beneath the Deep Probe-SAREX line further east.

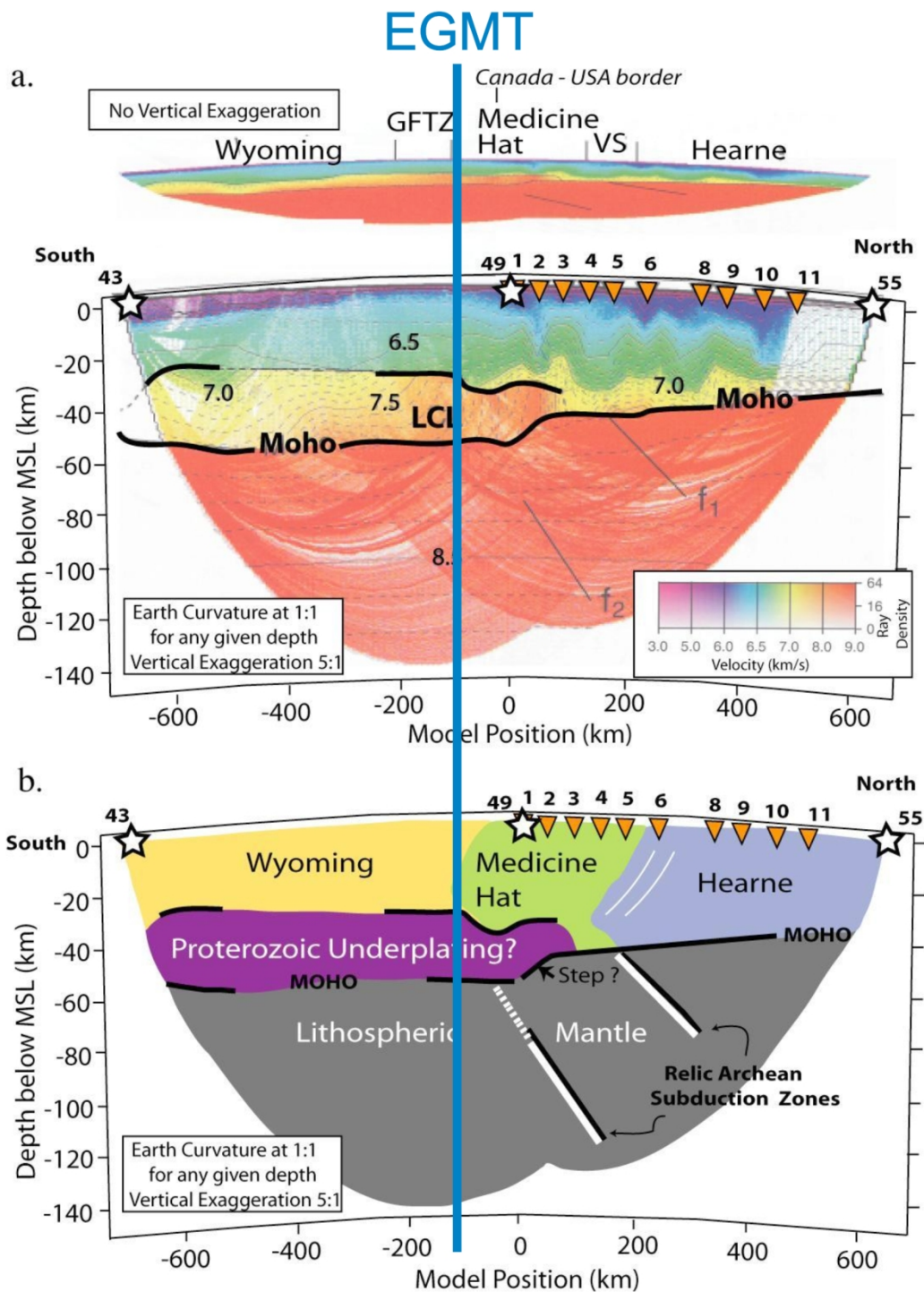


Figure 5-1. Location of EGMT along the Deep Probe-SAREX interpretation. A number of prominent features to the north, including massive folds, are likely the reason for the discrepancy in H values (modified from Gorman et al., 2002).

CHAPTER 6 CONCLUSIONS

Henstock et al. (1998) identified a fast LCL within the MHB, GFTZ, and WC and Gorman et al. (2002) interpreted it as a mafic layer due to a magmatic underplating event. Recent literature on Laurentia formation has begun to move away from the “stable Archean craton” train-of-thought and towards ideas of altering these thick crustal packages. Proterozoic underplating, including the presence of a LCL, could support this current thought process.

My study in this area has determined that a Proterozoic underplating event is plausible and a LCL could exist beneath some of the stations in this study. This interpretation depends on accepting the hypothesis of Ross (2002) that a single crustal thickening event occurred during the Proterozoic and minimal, if any, thickening occurred during the Sevier orogeny, Laramide orogeny, or other subsequent magmatic events. This hypothesis is derived from the interpreted xenoliths by Ross (2002), the lack of apparent structure of the LCL compared to the overlying cratons and terranes, and the postulated extend of this feature beneath multiple amalgamation territories. Seismic stations BOZ and MSO display thick crusts, 42.5 and 45.5 km, with high (> 1.9) V_p/V_s ratios. These stations therefore sit on continental crust with high V_p/V_s ratios consistent with a predominantly mafic crust (Holbrook et al., 1992). DGMT and LAO have low V_p/V_s ratios (< 1.7) typical of granitic (or felsic) continental crust. The Williston Basin sediments play little into these determinations, although they are clearly seen in the P-to- P_s phases of the seismograms (Holbrook et al., 1992; Tomlinson et al., 2006; Brauer et al., 2007).

Interpretation of the EGMT and RLMT RFs and structure is challenging because the RFs are complicated, probably due to the many significant Phanerozoic tectonic events that have affected crustal structure beneath RLMT, and potentially similar complicated structure at depth in the GFTZ beneath EGMT. RFs at EGMT are clearly different depending on event BAZ. Structure derived from one group of RFs is similar to that of BOZ and MSO, whereas the other group yields a lower V_p/V_s ratio and a thinner crust, closer to those at DGMT and LAO. The difference between the two results is likely caused by the variable BAZ groupings coupled with the suture zone location of the station. RLMT produced highly variable radial RFs with a strong peak in the transverse RFs (Figures 4-25 through 4-27). This is indicative of a dipping converter, although this structure does not appear in the interpretation by Gorman et al. (2002; Figure 1-1); it may exist but is not visible due to the poor resolution and large shot spacing on the US side of the survey.

The results of this study compare well with those of previous studies. The EARS results for DGMT and LAO are similar to my findings for crustal thickness and both projects involved RF estimations. Although BOZ and MSO are matched well with the CORE2.0 study, there is a fundamental difference between the Rocky Mountain and basin stations. The region in which BOZ and MSO are situated is much more complex due to a diverse tectonic history than the region for DGMT and LAO. Radial RF estimations are better suited for subhorizontal layers, making DGMT and LAO ideal for this type of study.

LIST OF REFERENCES

- Ammon, C.J., Randall, G.E., and Zandt, G., 1990, On the nonuniqueness of receiver function inversions: *Journal of Geophysical Research*, v. 95, no. 15, p. 303-318.
- Ammon, C.J., 1991, The isolation of receiver effects from teleseismic P waveforms: *Bulletin of the Seismological Society of America*, v. 81, no. 2, p. 504-510.
- Assumpção, M., James, D., and Snoke, A., 2002, Crustal thicknesses in SE Brazilian Shield by receiver function analysis: Implications for isostatic compensation: *Journal of Geophysical Research*, v. 107, ESE 2-1 – 2-14.
- Baird, D.J., Knapp, J.H., Steer, D.N., Brown, L.D., and Nelson, K.D., 1995, Upper-mantle reflectivity beneath the Williston basin, phase-change Moho, and the origin of intracratonic basins: *Geology*, v. 23, no. 5, p. 431-434.
- Bassin, C., Laske, G., and Masters, G., 2000, The current limits of resolution for surface wave tomography in North America: *EOS Trans AGU*, v. 81, F897.
- Berg, J. W. Jr., Trembly, L., Emilia, D. A., Hutt, J. R., King, J. M., Long, L. T., McKnight, W. R., Sarmah, S. K., Souders, R., Thiruvathukal, J. V., Vossler, D. A., 1966, Crustal refraction profile, Oregon coast range: *Bulletin of the Seismological Society of America*, v. 56, no. 6, p. 1357-1362.
- Bird, P., 1998, Kinematic history of the Laramide orogeny in latitudes 35-49N, western United States: *Tectonics*, v. 17, p. 780-801.
- Boerner, D., Craven, J., Kurtz, R., Ross, G., and Jones, F., 1998, The Great Falls tectonic zone: Suture or intracontinental shear zone?: *Canadian Journal of Earth Sciences*, v. 35, p. 175-183.
- Brauer, B., Ryberg, T., and Lindeque, A.S., 2007, Shallow seismic velocity structure of the Karoo Basin, South Africa: *South African Journal of Geology*, v. 110, p. 439-448.
- Brown, W.G., 1988, Deformational style of Laramide uplifts in the Wyoming foreland, Schmidt, C.J., and Perry, W.J., eds., *Interaction of the Rocky Mountain Foreland and the Cordilleran Thrust Belt*: Geological Society of America, memoir 171, p. 1-25.
- Carlson, R.W., Irving, A.J., Schulze, D.J., and Hearn Jr., B.C., 2004, Timing of Precambrian melt depletion and Phanerozoic refertilization events in the lithospheric mantle of the Wyoming Craton and adjacent Central Plains Orogen: *Lithos*, v. 77, p. 453-472.

- Cassidy, J.F., 1992, Numerical experiments in broadband receiver function analysis: Bulletin of the Seismological Society of America, v. 82, p. 1453-1474.
- Cassidy, J.F., 1995, A comparison of the receiver structure beneath stations of the Canadian National Seismograph Network: Canadian Journal of Earth Sciences, v. 32, p. 938-951.
- Chamberlain, K.R., and Frost, B.R., 1995. Mid-Proterozoic mafic dikes in the central Wyoming Province: evidence for Belt-age extension and supercontinent break-up: Geologic Association of Canada – Mineralogical Association of Canada, Abstracts, v. 20, A-15.
- Chamberlain, K.R., Frost, C.D., and Frost, B.R., 2003, Early Archean to Mesoproterozoic evolution of the Wyoming Province: Archean origins to modern lithospheric architecture: Canadian Journal of Earth Science, v. 40, p. 1357-1374.
- Chistiansen, R.L., and Yeats, R.S., 1992, Post-Laramide geology of the U.S. Cordillera region, in Burchfiel, B.C., Lipman, P.W., and Zoback, M.L., eds., The Cordilleran Orogen: Conterminous U.S.: Boulder, Colorado, Geological Society of America, The Geology of North America, v. G-3, chapter 7.
- Clowes, R.M., Burianyk, M.J.A., Gorman, A.R., and Kanesevich, E.R., 2002, Crustal velocity structure from SAREX, the Southern Alberta Refraction Experiment: Canadian Journal of Earth Sciences, v. 39, p. 351-373.
- Cowan, D.S., and Bruhn, R.L., 1992, Late Jurassic to early Late Cretaceous geology of the U.S. Cordillera, in Burchfiel, B.C., Lipman, P.W., and Zoback, M.L., eds., The Cordilleran Orogen: Conterminous U.S.: Boulder, Colorado, Geological Society of America, The Geology of North America, v. G-3, chapter 5.
- Crotwell, H.P., and Owens, T.J., 2005, Automated receiver function processing: Publications: SRL: Electronic Seismologist, http://www.seismosoc.org/publications/SRL/SRL_76/srl_76-6_es.html.
- Foster, D.A., Doughty, P.T., Kalakay, T.J., Fanning, C.M., Coyner, S., Grice, W.C., and Vogl, J., 2007, Kinematics and timing of exhumation of metamorphic core complexes along the Lewis and Clark fault zone, northern Rocky Mountains, USA: Geological Society of America Special Paper 434, p. 207-232, doi. 10.1130/2007.2434(10).
- Foster, D.A., Mueller, P.A., Mogk, D.W., Wooden, J.L., and Vogl, J.J., 2006, Proterozoic evolution of the western margin of the Wyoming craton: implications for the tectonic and magmatic evolution of the northern Rocky Mountains: Canadian Journal of Earth Science, v. 43, p. 1601-1619.

- Gorman, A.R., Clowes, R.M., Ellis, R.M., Henstock, T.J., Spence, G.D., Keller, G.R., Levander, A., Snelson, C.M., Burianyk, M.J.A., Kanesewich, E.R., Asudeh, I., Hajnal, Z., and Miller, K.C., 2002, Deep Probe: Imaging the roots of western North America: *Canadian Journal of Earth Science*, v. 39, p. 375-398.
- Henstock, T.J., and the Deep Probe Working Group, 1998, Probing the Archaean and Proterozoic lithosphere of Western North America: *GSA Today*, v. 8, p. 1-5.
- Holbrook, W.S., Mooney, W.D., and Christensen, N.J., 1992, The seismic velocity structure of the deep continental crust: *Continental Lower Crust Development in Geotectonics*, v. 23, p. 1-43.
- Humphreys, E., Hessler, E., Dueker, K., Farmer, G.L., Erslev, E., and Atwater, T., 2003, How Laramide-age hydration of North American lithosphere by the Farallon slab controlled subsequent activity in the western United States: *International Geology Review*, v. 45, p. 575-595.
- Johnson, S.H., and Couch, R.W., 1970, Crustal structure in the north Cascade mountains of Washington and British Columbia from seismic refraction measurements: *Bulletin of the Seismological Society of America*, v. 60, no. 4, p. 1259-1269.
- Keller, G.R., Karlstrom, K.E., and Farmer, G.L., 1999, Tectonic evolution in the Rocky Mountain region: 4-D imaging of the continental lithosphere: *Eos (Transactions, American Geophysical Union)*, v. 80, p. 493, 495, 498.
- Kirkwood, R., 2000, *Geology, Geochronology and economic potential of the Archean rocks in the western Owl Creek Mountains, Wyoming*: Unpublished, M.Sc. thesis, University of Wyoming, Laramide, Wyoming.
- Langston, C.A., 1977, Corvallis, Oregon, crustal and upper mantle receiver structure from teleseismic P and S waves: *Bull. Seism. Soc. America*, v. 67, p. 713-724.
- Langston, C.A., 1979, Structure under Mount Ranier, Washington, inferred from teleseismic body waves: *J. Geophys. Res.*, v. 84, p. 4749-4776.
- Latham, T.S., Best, J., Chaimov, T., Oliver, J., Brown, L., and Kaufman, S., 1988, COCORP profiles from the Montana plains: The Archean cratonic crust and a lower crustal anomaly beneath the Williston basin: *Geology*, v. 16, p. 1073-1076.
- Leighton, M. W., and Kolata, D. R., 1990, Selected interior cratonic basins and their place in the scheme of global tectonics: A synthesis, in Leighton, M. W., et al., eds., *Interior cratonic basins: American Association of Petroleum Geologists Memoir*, v. 51, p. 729-798.

- Ligorria, J.P., and Ammon, C.J., 1999, Iterative deconvolution and receiver-function estimation: *Bulletin of the Seismological Society of America*, v. 89, no. 5, p. 1395-1400.
- Levin, V., and Park, J., 1997, Crustal anisotropy in the Ural Mountains foredeep from teleseismic receiver functions: *Geophysical Research Letters*, v. 24, p. 1283-1286.
- Miller, D.M., Nilsen, T.H., and Bilodeau, W.L., 1992, Late Cretaceous to early Eocene geologic evolution of the U.S. Cordillera, in Burchfiel, B.C., Lipman, P.W., and Zoback, M.L., eds., *The Cordilleran Orogen: Conterminous U.S.: Boulder, Colorado, Geological Society of America, The Geology of North America*, v. G-3, chapter 6.
- Mjelde, R., Raum, T., Digranes, P., Shimamura, H., Shiobara, H., Kodaira, S., 2003. Vp/Vs ratio along the Vøring margin, NE Atlantic, derived from OBS data: implications on lithology and stress field: *Tectonophysics*, v. 369, p. 175–197.
- Mueller, P.A., Heatherington, A.L., Kelly, D.M., Wooden, J.L., and Mogk, D.W., 2002, Paleoproterozoic crust within the Great Falls tectonic zone: Implications for the assembly of southern Laurentia: *Geology*, v. 30, p. 127-130.
- O'Neill, J., 1998, The Great Falls tectonic zone, Montana-Idaho: An early Proterozoic collisional orogen beneath and south of the Belt Basin, in Berg, R.B., ed., *Belt Symposium III – 1993: Montana Bureau of Mines and Geology Special Publication 112*, p. 222-228.
- O'Neill, J., and Lopez, D., 1985, Character and regional significance of Great Falls tectonic zone, east-central Idaho and west-central Montana: *American Association of Petroleum Geologists Bulletin*, v. 69, p. 437-447.
- Ross, G.M., 2002, Evolution of Precambrian continental lithosphere in Western Canada: Results from Lithoprobe studies in Alberta and beyond: *Can. J. Earth Sci.*, v. 39, p. 413-437.
- Rumpfhuber, E.V., Keller, G.R., Sandvol, E., Velasco, A.A., and Wilson, D.C., 2009, Rocky Mountain evolution: Tying Continental Dynamics of the Rocky Mountains and Deep Probe seismic experiments with receiver functions: *Journal of Geophysical Research*, v. 114, B08301.
- Sheriff, S.D., and Stickney, M.C., 1984, Crustal structure of southwestern Montana and east-central Idaho: Results of a reversed seismic refraction line: *Geophysical Research Letters*, v. 11, p. 299-302.
- Snyder, G.L., Hughes, D.J., Hall, R.P., and Ludwig, K.R., 1989, Distribution of Precambrian mafic intrusive penetrating some Archean rocks of western North America: U.S. Geological Survey, Open-File Report 89-125.

- Stein, S., and Wysession, M., 2002, An Introduction to Seismology, Earthquakes and Earth Structure. 1st Edition. Wiley-Blackwell, pp. 498.
- Tanner, J.G., Aiken, C.L.V., Dehlinger, P., Dewhurst, W.T., de la Fuente, M., Godley, V.M., Godson, R.H., Hanna, W.F., Hildenbrand, T.G., Kleinkopf, M.D., McCaplin, G.A., McConnell, R.K., Meyers, H., O'Hara, N.W., Palmer, A.R., Scheibe, D.M., Sweeney, R.E., and Thorning, L., 1988, Gravity anomaly map of North America: *The Leading Edge*, v. 7, p. 15-18.
- Tomlinson, J.P., Denton, P., Maguire, P.K.H., and Booth, D.C., 2006, Analysis of the crustal velocity structure of the British Isles using teleseismic receiver functions: *Geophysical Journal International*, v. 167, p. 223-237.
- Zandt, G., and Ammon, C.J., 1995, Continental-crust composition constrained by measurements of crustal Poissons ratio: *Nature*, v. 374, p. 152-154.
- Zandt, G., Myers, S.C., and Wallace, T.C., 1995, Crust and mantle structure across the Basin and Range- Colorado Plateau boundary at 37°N latitude and implications for Cenozoic extensional mechanism: *Journal of Geophysical Research*, v. 100, p. 10529-10548.
- Zhu, L., 1993, Estimation of crustal thickness and Vp/Vs ratio beneath the Tibetan Plateau from teleseismic converted waves (abstract): *Eos Trans. AGU*, 74(16), Spring Meeting Supplement, p. 202.
- Zhu, L., and Kanamori, H., 2000, Moho depth variation in southern California from teleseismic receiver functions: *Journal of Geophysical Research*, v. 105, no. B2, p. 2969-2980.

BIOGRAPHICAL SKETCH

Robert Thomas Sirianni was born in Hornell, NY. He is the youngest child of Dorothy Nisbet and Daniel Sirianni. He has an older brother Daniel, and an older sister Cara. He attended elementary, middle, and high school in his hometown. Robert was accepted as a secondary education geology major at the State University of New York at Geneseo. After taking geology courses for two semesters he decided to switch and focus primarily on the geological sciences, rather than secondary education. He worked with Dr. Scott Giorgis on a senior thesis and completed the project during the spring semester 2007. During this time he became acquainted with computer programming as well as gained an interest in geophysics. Robert decided to attend the University of Florida where he worked with Dr. Ray Russo towards his Master of Science, concentrating in seismology. Upon completion of his master's degree, focused on using receiver functions to evaluate Moho depth across Montana, Robert intends to work for ExxonMobil starting in the spring 2010.